Monthly Notices of the ROYAL ASTRONOMICAL SOCIETY

MNRAS **530,** 3208–3227 (2024) https://doi.org/10.1093/mnras/stae1080
Advance Access publication 2024 April 23

IGM damping wing constraints on the tail end of reionization from the enlarged XQR-30 sample

B. Greig [1,2,3★] A. Mesinger [4] E. Bañados [5] G. D. Becker,[6] S. E. I. Bosman [5,7] H. Chen [8] F. B. Davies [5] V. D'Odorico [4,9,10] A.-C. Eilers [11] S. Gallerani,[4] M. G. Haehnelt,[12,13] L. Keating [14] S. Lai [15] Y. Qin [1,3] E. Ryan-Weber,[3,16] S. Satyavolu,[17] F. Wang,[18] J. Yang[18] and Y. Zhu [7,18]

[1]*School of Physics, University of Melbourne, Parkville, VIC 3010, Australia*
[2]*Research School of Astronomy & Astrophysics, Australian National University, Canberra, ACT 2611, Australia*
[3]*ARC Centre of Excellence for All-Sky Astrophysics in 3 Dimensions (ASTRO 3D)*
[4]*Scuola Normale Superiore, Piazza dei Cavalieri, I-56126 Pisa, Italy*
[5]*Max-Planck-Institut für Astronomie, Königstuhl 17, D-69117 Heidelberg, Germany*
[6]*Department of Physics and Astronomy, University of California, Riverside, CA 92521, USA*
[7]*Institute for Theoretical Physics, Heidelberg University, Philosophenweg 12, D-69120 Heidelberg, Germany*
[8]*Canadian Institute for Theoretical Astrophysics, University of Toronto, 60 St George St, Toronto, ON M5R 2M8, Canada*
[9]*INAF – Osservatorio Astronomico di Trieste, Via G.B. Tiepolo, 11, I-34143, Trieste, Italy*
[10]*IFPU – Institute for Fundamental Physics of the Universe, via Beirut 2, I-34151 Trieste, Italy*
[11]*MIT Kavli Institute for Astrophysics and Space Research, Massachusetts Institute of Technology, Cambridge, MA 02139, USA*
[12]*Institute of Astronomy, University of Cambridge, Madingley Road, Cambridge CB3 0HA, UK*
[13]*Kavli Institute of Cosmology, University of Cambridge, Madingley Road, Cambridge CB3 0HA, UK*
[14]*Institute for Astronomy, University of Edinburgh, Blackford Hill, Edinburgh, EH9 3HJ, UK*
[15]*Commonwealth Scientific and Industrial Research Organisation (CSIRO), Space & Astronomy, PO Box 1130, Bentley, WA 6102, Australia*
[16]*Centre for Astrophysics and Supercomputing, Swinburne University of Technology, Hawthorn, Victoria 3122, Australia*
[17]*Tata Institute of Fundamental Research, Homi Bhabha Road, Mumbai 400005, India*
[18]*Steward Observatory, University of Arizona, 933 N Cherry Ave, Tucson, AZ 85721, USA*

Accepted 2024 April 18. Received 2024 April 17; in original form 2024 April 1

ABSTRACT

The attenuation of Lyα photons by neutral hydrogen in the intergalactic medium (IGM) at $z \gtrsim 5$ continues to be a powerful probe for studying the epoch of reionization. Given a framework to estimate the intrinsic (true) Lyα emission of high-z sources, one can infer the ionization state of the IGM during reionization. In this work, we use the enlarged XQR-30 sample of 42 high-resolution and high signal-to-noise quasar spectra between $5.8 \lesssim z \lesssim 6.6$ obtained with VLT/X-shooter to place constraints on the IGM neutral fraction. This is achieved using our existing Bayesian QSO reconstruction framework which accounts for uncertainties such as the: (i) posterior distribution of predicted intrinsic Lyα emission profiles (obtained via covariance matrix reconstruction of the Lyα and N V emission lines from unattenuated high-ionization emission line profiles; C IV, Si IV + O IV], and C III]) and (ii) distribution of ionized regions within the IGM using synthetic damping wing profiles drawn from a 1.6^3 Gpc^3 reionization simulation. Following careful quality control, we used 23 of the 42 available QSOs to obtain constraints/limits on the IGM neutral fraction during the tail-end of reionization. Our median and 68th percentile constraints on the IGM neutral fraction are: $0.20^{+0.14}_{-0.12}$ and $0.29^{+0.14}_{-0.13}$ at $z = 6.15$ and 6.35. Further, we also report 68th percentile upper limits of $\bar{x}_{\rm H\,I} < 0.21$, 0.20, 0.21, and 0.18 at $z = 5.8$, 5.95, 6.05, and 6.55. These results imply reionization is still ongoing at $5.8 \lesssim z \lesssim 6.55$, consistent with previous results from XQR-30 (dark fraction and Lyα forest) along with other observational probes considered in the literature.

Key words: intergalactic medium – quasars: emission lines – dark ages, reionization, first stars – early Universe – cosmology: observations – cosmology: theory.

1 INTRODUCTION

The epoch of reionization (EoR) denotes the final major baryonic phase change of the Universe, when the pervasive cold and dense neutral hydrogen fog in the intergalactic medium (IGM) is evaporated by the intense glow of ultraviolet (UV) ionizing radiation from the first sources. The morphological evolution of the IGM proceeds in a patchy manner whereby individual ionized (H II) regions form first around the earliest structures before growing and merging with their nearest neighbours, percolating and eventually ionizing almost all of the neutral hydrogen in the IGM. Observing and subsequently

★ E-mail:greigb@unimelb.edu.au

characterizing the EoR is of fundamental importance as it will advance our knowledge of the nature of the first structures to form in the Universe.

Our most promising observational tool for probing the EoR is the detection of the 21-cm hyperfine spin-flip transition of neutral hydrogen via radio interferometry. However, this continues to remain elusive with the best-yet upper limits on the 21-cm signal (Mertens et al. 2020; Trott et al. 2020; Abdurashidova et al. 2022a) still a few orders of magnitude away from our theoretical expectations (Ghara et al. 2020, 2021; Greig, Mesinger & Koopmans 2020; Mondal et al. 2020; Greig et al. 2021; Abdurashidova et al. 2022b; HERA Collaboration 2023).

In the absence of directly measuring the neutral hydrogen in the IGM, we can instead infer its presence via its impact on the Lyα photons emitted by bright astrophysical sources such as galaxies and QSOs. At lower redshifts, one can directly infer the ionization state of the IGM by measuring the absorption of Lyα photons within the Lyα forest along the line of sight from the source. However, at $z \gtrsim 5$ the scattering cross-section of Lyα photons is sufficiently large that even trace amounts of neutral hydrogen ($x_{\rm H\,I} \gtrsim 10^{-4}$) are enough to produce completely saturated transmission (Fan et al. 2006). As a result, fluctuations in the neutral fraction owing to the patchy nature of reionization are almost indistinguishable from fluctuations post-reionization of the UV background, density or temperature (e.g. D'Aloisio, McQuinn & Trac 2015; Keating, Puchwein & Haehnelt 2018). However, physical models predict different large-scale fluctuations and biases of these fields, which can be used to constrain the EoR history and galaxy properties (see e.g. fig. 2 in Qin et al. 2021).

Alternatively, a more robust probe of the IGM neutral fraction is to measure the imprint of the Lyα damping wing (e.g. Rybicki & Lightman 1979; Miralda-Escudé 1998). This approach takes advantage of the Lorentzian wings away from the resonant central core of the Lyα absorption cross-section. In these wings, the amplitude of the scattering cross-section is several orders of magnitude lower and imprints a smooth absorption profile away from the central saturated absorption. Thus, even a completely neutral IGM will impart a smooth, measurable imprint in the transmission spectrum of the background source sufficiently redward from the line centre.

This IGM damping wing signature has been successfully measured to obtain constraints on the IGM neutral fraction using both galaxies and QSOs. For QSOs, their intrinsic brightness allows the damping wing imprint to be inferred from individual spectra (e.g. Mesinger & Haiman 2007; Bolton et al. 2011; Mortlock et al. 2011; Greig et al. 2017b; Bañados et al. 2018; Davies et al. 2018a; Wang et al. 2020; Yang et al. 2020). On the other hand, for galaxies, the extraction of the damping wing signal requires averaging over a sufficiently large statistical sample owing to the fainter nature of galaxies (e.g. Mesinger et al. 2015; Mason et al. 2018, 2019; Hoag et al. 2019; Umeda et al. 2023), however, it can be more difficult to distinguish the IGM component from the host galaxy environment than is the case for QSOs (e.g. Heintz et al. 2023; Keating et al. 2023, 2024).

Importantly, the key requirement for extracting the IGM damping wing imprint is a robust method to predict the intrinsic Lyα emission, given we inherently observe an attenuated spectrum. For QSOs, numerous methods exist in the literature which differ considerably in their methodology (e.g. Davies et al. 2018b; Fathivavsari 2020; Reiman et al. 2020; Ďurovčíková et al. 2020; Bosman et al. 2021; Liu & Bordoloi 2021; Chen et al. 2022; Sun, Ting & Cai 2023) but fundamentally boil down to predicting the Lyα profile from unattenuated spectral information redward of Lyα. In Greig et al. (2024), a detailed comparison of the various reconstruction pipelines in the literature, focusing on the reconstruction of the Lyα line profile, are performed as part of a blind reconstruction challenge. This extends on the work of Bosman et al. (2021), comparing methods to predict the placement of the Lyα forest continuum.

In this work, we use the Bayesian reconstruction pipeline initially introduced in Greig et al. (2017a) which predicts the intrinsic Lyα profile by drawing from an N-dimensional normal distribution with a covariance matrix containing the correlations between the Lyα and N V line and the unattenuated high-ionization emission lines (C IV, Si IV + O IV], and C III]). This approach assumes that the emission lines can be modelled as either a single or double component Gaussian profile characterized entirely by the width, height, and velocity offset. We then couple this reconstruction framework to distributions of synthetic IGM damping wings drawn from a large-volume EoR simulation (Mesinger, Greig & Sobacchi 2016). In doing so, we account for the statistical uncertainties that arise since we are using single lines of sight to each QSO spectra to place constraints on the volume averaged IGM neutral fraction during the EoR.

Previously, IGM damping wing analyses have focused solely on the highest redshift QSOs to be discovered at $z \gtrsim 7$ (Mortlock et al. 2011; Bañados et al. 2018; Wang et al. 2020; Yang et al. 2020).[1] However, in this work we take advantage of the Ultimate X-shooter legacy survey of QSOs at $5.8 \lesssim z \lesssim 6.6$, XQR-30 (D'Odorico et al. 2023). This programme obtained 30 high signal-to-noise (S/N) QSO spectra at high resolution ($\sim$30 km s^{-1}). These were supplemented by a further 12 high-quality $z \sim 6$ QSOs from the X-shooter archive to produce a final sample of 42 QSOs. The sheer size of this QSO sample and the corresponding redshift coverage will enable unique constraints on the tail end of the EoR to be recovered.

This work is structure as follows. In Section 2, we provide a brief description of the observational data, and in Section 3, we describe our full analysis pipeline. In Section 4, we provide the main results along with detailed discussions. In Section 5, we conclude with our closing remarks. Unless stated otherwise, we quote all quantities in co-moving units and adopt the cosmological parameters: (Ω_Λ, $\Omega_{\rm M}$, Ω_b, n, σ_8, H_0) = (0.69, 0.31, 0.048, 0.97, 0.81, 68 km s^{-1} Mpc^{-1}), consistent with recent results from the *Planck* mission (Planck Collaboration XIII 2016).

2 DATA

2.1 Sample

The data used in this work come from the XQR-30 sample (D'Odorico et al. 2023), which is an ESO (European Southern Observatory) Large Programme 'XQR-30: the Ultimate X-shooter legacy survey of quasars at $z \simeq 5.8$–6.6 arcsec (PI: V. D'Odorico; 1103.A-0817). Targeting 30 of the brightest known QSOs within this redshift range with X-shooter (Vernet et al. 2011), we obtained a median resolution of $R \sim 9500$–13 700 in the visible arm and $R \sim 7600$–11 000 in the near-infrared arms. For this work, we rebinned the observed QSO spectra to 50 km s^{-1}. In addition to these 30 QSOs, a further 12 QSOs with similar redshift range, magnitude, resolution, and S/N to the original XQR-30 sample were added from the X-shooter archive to yield the enlarged XQR-30 sample. This entire sample was reduced using a custom pipeline (López et al. 2016; Becker et al. 2019), with minor modifications made for XQR-30 (see D'Odorico et al. 2023, for further details).

[1] Although, see Ďurovčíková et al. (2024) who very recently performed an analysis of a much larger sample of 18 QSOs from $6.0 < z < 7.1$.

Table 1. A summary of the enlarged XQR-30 data set. Columns correspond to the QSO name, redshift, emission line used for obtaining the redshift, recovered IGM neutral fraction (68 percentiles, either represented as an upper limit or constraint) and brief comments highlighting the reason for each QSOs exclusion or retention (see the main text for further details).

QSO name	Redshift (z)	Redshift method	$\bar{x}_{\rm H\,I}$	Comments
PSO J029 − 29	5.976	Mg II	<0.22	
VST-ATLAS J029 − 36	6.013	Mg II	<0.40	
VDES J0224 − 4711	6.525	Mg II	<0.33	
PSO J060 + 24	6.170	Mg II	$0.29^{+0.24}_{-0.19}$	
VDES J0408 − 5632	6.033	Mg II	$0.24^{+0.19}_{-0.15}$	Mini BAL or weak BAL[a]
PSO J108 + 08	5.955	Mg II	<0.31	
SDSS J0842 + 1218	6.0754	[C II]	<0.30	Mini BAL or weak BAL[a]
PSO J158 − 14	6.0685	[C II]	<0.32	
PSO J217 − 16	6.1498	[C II]	$0.29^{+0.20}_{-0.18}$	
PSO J231 − 20	6.5869	[C II]	<0.29	Mini BAL or weak BAL[a]
PSO J242 − 12	5.840	Mg II	<0.25	
PSO J308 − 27	5.799	Mg II	$0.33^{+0.22}_{-0.20}$	
PSO J323 + 12	6.5872	[C II]	$0.23^{+0.19}_{-0.15}$	
PSO J359 − 06	6.1722	[C II]	<0.34	
SDSS J0100 + 2802	6.3269	[C II]	$0.41^{+0.19}_{-0.18}$	
VST-ATLAS J025 − 33	6.3373	[C II]	<0.33	
ULAS J0148 + 0600	5.977	Mg II	$0.32^{+0.23}_{-0.20}$	Mini BAL or weak BAL[b]
PSO J036 + 03	6.5405	[C II]	<0.31	
SDSS J0836 + 0054	5.773	Mg II	<0.33	
SDSS J0927 + 2001	5.7722	[C II]	<0.33	
SDSS J1030 + 0524	6.304	Mg II	<0.40	
SDSS J1306 + 0356	6.0330	[C II]	<0.36	
CFHQS J1509 − 1749	6.1225	[C II]	<0.38	
PSO J007 + 04	6.0015	[C II]	–	pDLA
PSO J009 − 10	6.0040	[C II]	–	BAL
PSO J023 − 02	5.817	Mg II	–	BAL, pDLA
PSO J025 − 11	5.816	Mg II	–	pDLA
PSO J065 − 26	6.1871	[C II]	–	pDLA
PSO J065 + 01	5.804	Mg II	–	Mini BAL or weak BAL
PSO J089 − 15	5.972	Mg II	–	BAL
J0923 + 0402	6.6330	[C II]	–	BAL
PSO J183 + 05	6.4386	[C II]	–	pDLA
PSO J183 − 12	5.893	Mg II	–	Mini BAL or weak BAL
PSO J217 − 07	6.166	Mg II	–	BAL
DELS J1535 + 1943	6.358	Mg II	–	Heavily reddened
PSO J239 − 07	6.1102	[C II]	–	BAL, pDLA
VDES J2211 − 3206	6.3394	[C II]	–	BAL
VDES J2250 − 5015	5.985	Mg II	–	BAL
SDSS J2310 + 1855	6.0031	[C II]	–	Mini BAL or weak BAL, pDLA
WISEA J0439 + 1634	6.5188	[C II]	–	BAL
SDSS J0818 + 1722	5.960	Mg II	–	pDLA
ULAS J1319 + 0950	6.1347	[C II]	–	pDLA

Note.[a] Although identified as a possible mini/weak BAL by Bischetti et al. (2023), the associated BAL complex does not impact the Lyα + N V emission line complex. [b] A potential weak BAL complex however the large blueshift should not contaminate the Lyα + N V emission line complex (Becker et al. 2015).

2.2 Final damping wing sample

Unfortunately not all of the 42 QSOs from the enlarged XQR-30 sample can be used for IGM damping wing studies. For example, we must avoid QSOs which exhibit absorption by dense, neutral absorption systems in close proximity to the host QSO (e.g. damped Lyα systems; DLAs) which produce their own damping wing imprint which can imitate the damping wing signal from a partially neutral IGM (e.g. Prochaska, Hennawi & Herbert-Fort 2008; Bañados et al. 2019; Davies et al. 2023). Further, QSOs which exhibit broad absorption lines (BALs) must also be excluded as these lines either contaminate the observed flux around Lyα and N V or impact our ability to accurately measure the continuum and emission line properties of the QSOs redward of Lyα which are pre-requisite for our intrinsic Lyα reconstruction pipelines. In Table 1, we summarize the full XQR-30 sample, highlighting which QSOs are retained for our damping wing studies, and discuss the exclusions of certain objects in greater detail below.

Bischetti et al. (2022) performed an extensive C IV BAL analysis of the XQR-30 sample, with a follow up analysis exploring N V, Si IV + O IV], and Mg II BAL systems (Bischetti et al. 2023). Following this, 14 BAL QSOs were identified. However, of these, three (VDES J0408 − 5632, SDSS J0842+1218, and PSO J231 − 20) were deemed suitable for our damping wing analysis as the velocities of the BAL systems do not contaminate the Lyα + N V line complex. In D'Odorico et al. (in preparation) proximate DLA systems (pDLAs) have been identified within 7 of the XQR-30 QSOs, however only four of these are unique (i.e are not also identified as BAL QSOs). We further exclude the heavily reddened QSO J1535 + 1943, which is thought to be obscured (Yang et al. 2021).

Of the additional 12 archival X-shooter spectra in the XQR-30 sample, two exhibit pDLA systems (J0818 + 1722 and J1319 + 0950). Further, J0439 + 1634 is known to exhibit a BAL system. J0148 + 0600 also likely exhibits a BAL system (Becker et al. 2015) however it is highly blueshifted and should not contaminate the Lyα + N V line complex.

In total, this results in 23 QSOs from the XQR-30 sample that we deem suitable for extracting the IGM damping wing imprint.

3 METHOD

Our damping wing analysis relies on the covariance matrix reconstruction pipeline introduced by Greig et al. (2017a) and subsequently extended in Greig et al. (2022) in order to simultaneously reconstruct the Lyα and N V emission lines. This is combined with a Bayesian sampling of synthetic IGM damping wing profiles drawn from large-volume EoR simulations to be able to infer the IGM neutral fraction. Below, we summarize the key components of our full analysis pipeline and refer the reader to the aforementioned works for more in-depth discussions.

3.1 Intrinsic Lyα profile reconstruction

In Greig et al. (2017a), we introduced a method to reconstruct the intrinsic Lyα line profile of QSOs using a covariance matrix of correlations between Lyα and other measurable high-ionization lines (namely, C IV, Si IV + O IV], and C III]). This covariance matrix was determined from a carefully selected (visually inspected) training set of 1673 moderate-z ($2.08 < z < 2.5$), high S/N (>15) QSOs from the Sloan Digital Sky Survey (SDSS-III) Baryon Oscillation Spectroscopic Survey (BOSS) DR12 (Dawson et al. 2013; Alam et al. 2015) to avoid the presence of BAL and DLA systems. In Greig et al. (2022), we expanded the emission line covariance matrix to allow the simultaneous reconstruction of Lyα and N V.

The underlying assumption of this pipeline is that each emission line can be modelled by a sum of Gaussian profiles, each fully described by its amplitude, width, and velocity offset away from systemic. In Greig et al. (2017a), we performed basic model selection to determine that the Lyα and C IV line profiles are best characterized by a two-component Gaussian, consisting of both a broad and narrow component. In addition to the Gaussian emission lines, we model the QSO continuum as a single two-parameter power law ($\propto \lambda^{\alpha_\lambda}$) over our entire fitting region (1180–2300 Å) and normalize all QSO spectra to unity at 1450 Å. For all remaining emission lines, a single-component Gaussian profile was preferred.[2] This results in a 21 × 21 covariance matrix of emission line parameters that is used to construct a 21D Normal distribution which describes the full properties of our five emission lines. The two parameters describing the power-law continuum do not enter the covariance matrix as they do not correlate with the parameters describing the emission lines.

3.1.1 Enlarged QSO training set

For this work we significantly expand our original training set of QSOs, updating our training set to use the BOSS DR16Q database (Lyke et al. 2020). We both expand the redshift range from our original $2.08 < z < 2.5$ to a broader $2.08 < z < 4.0$ and reduce our S/N cut down from S/N >15 to >6.5. Owing to this expansion of the training set, we now forego visual inspection of the QSOs in our training set. The primary reason for expanding this training set is twofold: (i) to avoid biasing our training set based on the quality of QSO spectra (large amplitude Lyα peaks etc.) and (ii) to increase the sampled distribution of emission line parameters to ensure a larger region of validity for our covariance matrix.

After broadening our training set, we are left with ∼55 000 QSOs. We then reduce this sample further by removing QSOs with too many coincident absorption features[3] around our emission lines which can make determining the true profile problematic. Thus, we restrict our sample to QSOs with fewer than 20 absorption features across our fitting range of 1180–2300 Å and fewer than 8 in the 1180–1260 Å region around Lyα and N V. While these choices are arbitrary, they strike a balance between providing a sufficient number of QSOs for evaluating our covariance matrix and limiting the number of outlier spectra. Note, in fitting these absorption features we do not distinguish by their origin (i.e. Lyα forest, intervening metal absorption and/or QSO associated absorption). Simply, from experience we find that for an increasing number of individual absorption lines within the 1180–1260 Å region, determining the intrinsic Lyα profile from the training QSOs becomes problematic as the Lyα components become strongly degenerate with these numerous absorption features. Beyond just the Lyα region, we additionally find that too many absorption lines can impact our ability to fit the two component power-law continuum, impacting all subsequent emission line fits. After these cuts, our final training set consists of 30 166 QSOs, corresponding over an order of magnitude increase from the 1673 QSOs used in Greig et al. (2017a). In Appendix A, we provide the correlation coefficient matrix demonstrating the various emission line correlation strengths. With such a large number of QSOs in the training set, it is unlikely that our resultant correlations will be strongly biased. Interestingly, despite substantially increasing the size of our QSO training set for this work, we find very similar correlations strengths between our emission lines as we have found previously (Greig et al. 2022). Although the correlation strengths remain similar, the notably larger training set demonstrates that these line correlations exist over broader ranges for the individual emission line parameter properties.

[2]Note, we fit all observed emission lines that fall within this specific wavelength region, but only use the high-ionization lines for the covariance matrix. That is, we also simultaneously fit for the following lines Si II, O I/Si II, C II, He II, O III/Al II/Fe II, and Al III (see Greig et al. 2017a for further details). Further, we do not consider an emission component from an Fe continuum, however, for the purposes of our studies we find such a component unlikely to impact on our QSO fits.

[3]Absorption features are identified through an automated procedure based on a rolling 2 Å window, flagging all flux bins below 3σ (5σ around Lyα) and then roughly determining the absorber line centre which is assigned a Gaussian profile (see Greig et al. 2017a for further details). All absorption features are simultaneously fit to the QSO spectrum along with the emission lines, varying their width, amplitude and velocity offset.

3.1.2 Reconstruction pipeline for XQR-30

With our updated covariance matrix of emission line parameters, we now outline our method for reconstructing the intrinsic Lyα and N V emission lines. The key steps are as follows:

(i) The observed rest-frame QSO spectrum is fit over $\lambda = 1275$–2300 Å using the systemic QSO redshifts[4] outlined in Table 1.

(ii) We jointly fit the two-parameter power-law continuum and the high-ionization lines Si IV + O IV], C IV (two-component) and C III] emission line profiles using our Gaussian profiles. Additionally, to improve the overall fit to the observed spectrum, we simultaneously allow a variable number of absorption lines, each modelled as a single Gaussian profile, to be fit.

(iii) Using the corresponding fits to the C IV, Si IV + O IV], and C III] emission lines (amplitude, width, and velocity offset) of our observed high-z QSO spectrum, we use the maximum *a*-posteriori values for these lines and evaluate our 21D Normally distributed covariance matrix model. This allows us to reduce the full 21-parameter model down to a 9D estimate of just the joint Lyα and N V intrinsic emission line profile (two Gaussian components for Lyα and one for N V).

(iv) We then draw joint intrinsic Lyα and N V profiles from this 9 dimensional covariance matrix. We further utilize the amplitude of the observed spectrum redward of 1250 Å as an additional prior, to ensure the reconstructed profiles match the observed flux within this range.

3.2 Modelling the IGM damping wing during reionization

In order to extract the imprint of a partially neutral IGM, we compare the observed signal against our intrinsic profile reconstructions convolved with synthetic IGM damping wing profiles. Our synthetic IGM damping wing profiles are obtained from the Evolution of 21-cm Structure (Mesinger et al. 2016)[5] 2016 simulations. These semi-numerical reionization simulations have side lengths of 1.6 Gpc over 1024 voxels and include state-of-the-art subgrid prescriptions for inhomogeneous recombinations and the photoheating suppression of star formation. Further, through judicial choices of star formation efficiency and the typical masses of haloes hosting star-forming galaxies, three distinct EoR morphologies are explored.

Following Greig et al. (2022), we only consider the INTERMEDIATE H II model, which corresponds to reionization driven by galaxies residing in $M_h \gtrsim 10^9$ M$_\odot$ haloes.[6] This model is consistent with recent results from forward modelling the Lyα forest opacity distributions and UV galaxy luminosity functions (LFs; Qin et al. 2021).

We statistically account for the fact we only obtain a single observed QSO sightline by drawing a large sample of synthetic IGM damping wing profiles varying both: (i) the sightline orientation (selecting 10 different lines of sight through the IGM centred on the host halo) and (ii) the diversity of host QSO environments in the IGM. In total, we draw 10^5 synthetic IGM damping wing profiles obtained from the 10^4 largest identified haloes (corresponding to roughly $6 \times 10^{11} < M_h < 3 \times 10^{12}$ M$_\odot$)[7] and 10 randomly oriented sightlines originating from the central host halo. To have these synthetic damping wing profiles varied by IGM neutral fraction we take the ionization fields obtained from different redshift snapshots from the simulation, which assumes the halo locations do not significantly change due to bulk motions across the different redshift snapshots. Following this, we obtain 24 unique, unevenly spaced values of the IGM neutral fraction, corresponding to the original redshift sampling of our seminumerical simulations (i.e. 24 different snapshots during the EoR), spanning from $\bar{x}_{\rm H\,I} = 0.02$ to 0.95 for our analysis.

These synthetic damping wing profiles are constructed by assuming a minimum local H II bubble size, $R_{\rm min}$, which for the $z > 7$ QSOs (Greig et al. 2017b; Greig et al. 2019; Greig et al. 2022) was adopted to be their corresponding proximity zone size. This is necessary since within our EoR simulations we do not model the impact that the QSO has on growing its own local H II bubble. The actual size of the local H II region is the combination of the cumulative ionizing output of the resident local galaxies (which is incorporated within our simulations) and the unknown QSO contribution, which is crudely implemented by assuming that at a minimum this QSO plus galaxy contribution has to have at least ionized the size of the measured QSO proximity zone. The contribution of the QSO to the local H II region is strongly dependent on its accretion history, obscuration and emission geometry all of which are highly uncertain and thus difficult to impose physically motivated priors. Therefore, in this work we only search for the IGM damping wing imprint between $\lambda = 1218$–1230 Å to specifically avoid having to simultaneously model the host QSO environment blueward of Lyα, thus minimizing additional modelling uncertainties. This choice makes our approach more agnostic to the QSO emission model and its associated priors. The lower bound of 1218 Å ensures we are sufficiently far from the gravitational potential of the halo, avoiding potential signatures of inflowing gas. This approach differs to that of Davies et al. (2018a) who utilize numerical simulations to develop a hybrid scheme allowing for the search of the damping wing imprint over an extended region of $\lambda \sim 1190$–1230 Å. This enables these QSO emission model uncertainties such as the QSO lifetime and environment to be folded into their analysis. A detailed discussion of the consequences of these assumptions are provided in Greig et al. (2022) but in summary our redward approach implicitly imposes a complex prior on the QSO lifetime, but should not strongly impact our results on the inferred neutral fraction. A quantitative estimate of the impact of this prior is beyond the scope of this work, as it requires a detailed comparison of the two different damping wing extraction methods.

Due to the significantly increased number of QSOs in the XQR-30 sample relative to our previous $z > 7$ QSO studies and the additional computational burden of having to regenerate these synthetic sightlines for each possible $R_{\rm min}$, we instead choose to only use the existing synthetic damping wing profiles from the four previously analysed $z > 7$ QSOs. Therefore, for each XQR-30 QSO we simply average over our existing data, drawing 10^5 profiles for $R_{\rm min}$; ∼11–16

[4]Note, our BOSS QSO training set is converted to rest frame using the provided pipeline redshift, rather than the [C II] or Mg II redshifts of the XQR-30 sample. Although this may lead to biases in the reconstructions due to differences in the obtained red/blueshifts from systemic, this is likely a subdominant effect relative to the large scatter in the reconstructed Lyα + N V line and of the synthetic IGM damping wings (see Greig, Mesinger & Bañados 2019, for detailed discussions)

[5]http://homepage.sns.it/mesinger/EOS.html

[6]In Greig et al. (2019), we explored the impact that different EoR morphologies had on the recovered IGM neutral fraction constraints, finding only weak evidence for morphology dependence. The median IGM neutral fraction due to the different EoR morphologies was found to be only ±0.05 relative to the typical 68th percentile uncertainty of ±0.15–0.20. This should not impact our results in any discernible way.

[7]Although the XQR-30 QSOs are known to be bright and powered by massive blackholes (Mazzucchelli et al. 2023), they are consistent with the range of halo masses considered within our seminumerical simulations and thus should not strongly impact on our inferred constraints on the IGM neutral fraction.

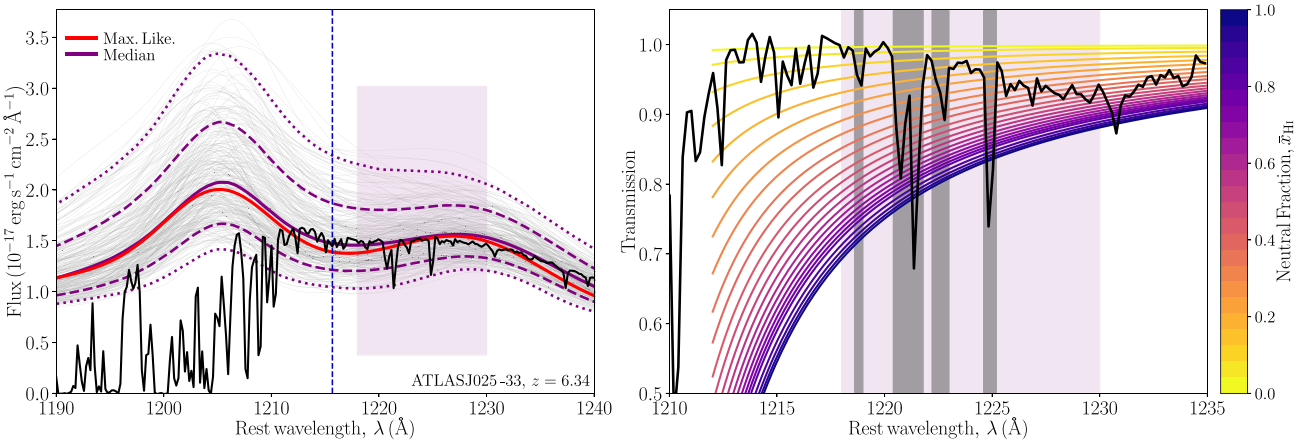

Figure 1. A visual demonstration of the initial covariance reconstruction for ATLAS J025 − 33 at $z = 6.34$ highlighting problems with our original reconstruction pipeline. Left panel: the observed QSO spectrum (black curve), corresponding ML (red curve) reconstruction and 300 random profile draws (grey curves) from our full reconstructed covariance matrix. The solid purple curve corresponds to the median reconstruction profile obtained from the full distribution of reconstructed profiles while the dashed (dotted) curves correspond to the 68th (95th) distribution of profiles. The vertical blue dashed line corresponds to rest-frame Lyα, while the purple box denotes the region over which we fit for the IGM damping wing imprint (1218–1230 Å). Right panel: the observed Lyα transmission profile (black curve) obtained by dividing the observed spectrum by the median reconstructed profile. The coloured lines correspond to the median synthetic IGM damping wing profiles for each IGM neutral fraction value sampled by our EoR simulations. Grey-shaded regions correspond to absorption features that are masked by our damping wing fitting pipeline.

comoving Mpc.[8] By averaging over these $R_{\rm min}$ we effectively broaden our resultant posteriors, leading to a more conservative estimate of the IGM neutral fraction. In Appendix B, we explore the impact of assuming different $R_{\rm min}$ for one of our QSOs in our sample. Between our lower and upper limits on this minimum radii we find the inferred IGM neutral fraction shifts by ∼0.02, which is considerably smaller than the width of the resultant posterior. Therefore, this choice of convolving over $R_{\rm min}$ should have little impact on our inferred results on the IGM neutral fraction.

3.3 Initial QSO reconstruction performance

Our initial attempts at performing intrinsic reconstructions following the procedure outlined in Section 3.1.2 for the XQR-30 sample proved to be problematic. As a visual demonstration, in the left panel of Fig. 1 we provide our initial attempt at reconstructing the intrinsic profile of ATLAS J025 − 33. The black curve corresponds to the observed spectrum, while the red line corresponds to the maximum-likelihood (ML) profile reconstruction. The grey lines correspond to 300 random posterior draws of our reconstructed profiles, while the purple solid line corresponds to the median profile and the dashed (dotted) purple lines demarcate the 68th and 95th percentile ranges determined over the full distribution of reconstructed profiles. Finally, the purple-shaded box corresponds to the interval over which we extract the smooth IGM damping wing component (1218–1230 Å).

In this example, the ML reconstruction (also the median, but to a lesser extent as it is obtained over the distribution instead of an individual profile) drops below the observed spectrum between rest-frame 1210–1220 Å.[9] Owing to the strong blueshift of this particular QSO, this corresponds to the flux between the Lyα and N v emission lines. Importantly, this 'feature' is not just restricted to one QSO, instead it is persistent across the full QSO sample, systematically occurring between the Lyα and N v emission lines. In the right panel of Fig. 1, we demonstrate the impact that this behaviour can have on our recovery of the smooth IGM damping wing imprint. Here, we show the Lyα transmission profile (black curve), obtained by dividing the observed spectrum (black curve, left panel) by the median reconstruction profile (purple curve, left panel). The coloured curves correspond to the median synthetic IGM damping wing profiles for each value of the IGM neutral fraction sampled by our dataset (increasing neutral fraction from top to bottom, see Section 3.2). The smooth, monotonically increasing synthetic damping wing profiles are incompatible with the decreasing amplitude of the observed Lyα transmission within the 1218–1230 Å region owing to this underestimate of the intrinsic flux. Attempting to jointly fit the observed Lyα transmission and synthetic damping wing profiles within this region was problematic for our pipeline.

3.4 Calibrating our QSO reconstruction pipeline

We initially assumed that the origin of this feature was the higher quality of the X-shooter sample relative to the training set of SDSS (BOSS) QSOs used in the construction of our covariance matrix. The higher resolution would then lead to more prominent emission line features (less blended), in particular around Lyα and N v driving this difference. Subsequently, we degraded the XQR-30 QSOs to better mimic the spectral properties of the QSOs within our training set but

[8]Note that this is slightly smaller than some of the proximity zone sizes measured for the XQR-30 sample by Satyavolu et al. (2023); 2–7 proper Mpc at $z = 5.8$–6.6. However, unfortunately we no longer have the base simulation data to extend our upper limit of $R_{\rm min}$. Nevertheless, this should not significantly impact our results due to the broad range of modelling uncertainties.

[9]The reconstructed profile also drops below the observed spectrum at >1235 Å, however, this is less prevalent across our sample and occurs outside of the region over which we fit for the damping wing (i.e. 1218–1230 Å). Nevertheless, this likely is related to the issues with the width and placement of the N v line from our reconstructed profile.

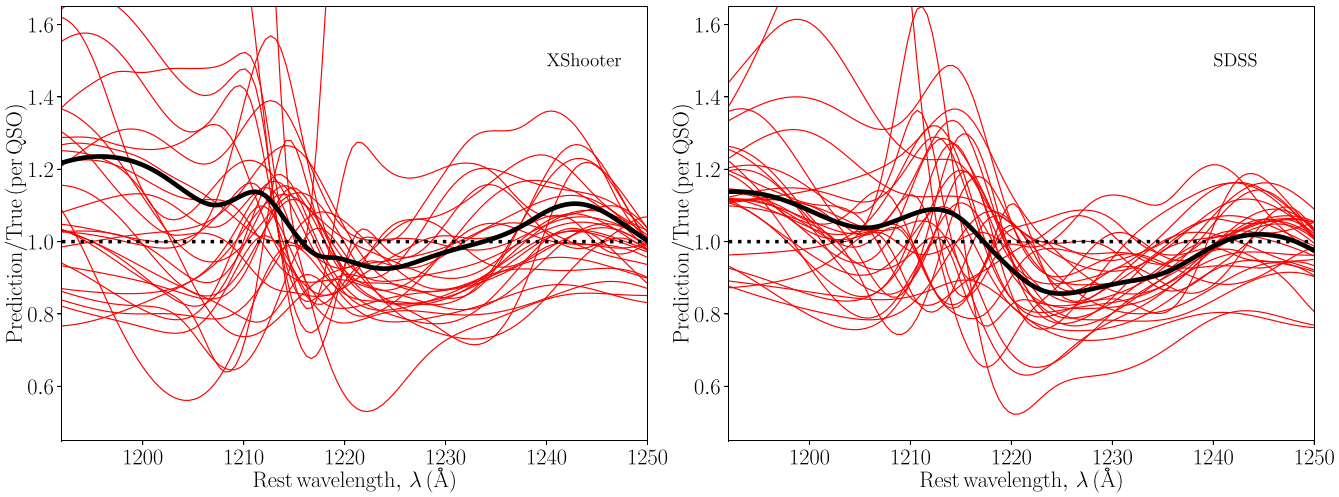

Figure 2. The performance of our covariance matrix reconstruction method from two distinct samples of 30 QSOs from X-shooter (left panel) and SDSS (BOSS; right panel) at $3.5 < z < 4.5$. The red solid lines correspond to the flux ratio (reconstructed ML profile over true intrinsic profile) for each individual QSO in the samples. The black solid lines correspond to the median determined over each sample.

found that this behaviour of a reduction of flux between Lyα and N V persisted.

Therefore, in order to establish the origin of this feature in our profile predictions we performed a reconstruction of QSOs drawn from two different samples both at $3.5 < z < 4.5$ which should be unaffected by IGM attenuation (i.e. where we can easily establish the true intrinsic profile shape). For this, we constructed two samples of 30 QSOs each, one observed with X-shooter to obtain QSOs of similar quality and properties of the XQR-30 sample and one with SDSS (BOSS DR16Q)[10] to be representative of the quality of our training set spectra. For the former, we utilize the XQ100 sample (López et al. 2016). Importantly, by considering two samples of QSOs from distinctly different instruments, we can determine whether: (i) the problems in our reconstruction are intrinsic to the quality of the spectrum and (ii) whether it is acceptable for a reconstruction method trained on lower quality spectra to be applied to any instrument.

Originally, the scope of this investigation was to be limited to just our covariance matrix reconstruction pipeline. However, it quickly morphed into a robust and detailed comparison of all available reconstruction pipelines in the literature. For detailed discussions resulting from this comparison, we refer the reader to Greig et al. (2024). In short, the issue was identified to be intrinsic to our covariance reconstruction method (see below) and that the quality of the spectra in the training set (e.g. resolution or S/N) relative to the observed spectra did not impact the reconstruction performance. In the remainder of this section, we focus only on the results intrinsic to our covariance matrix reconstruction pipeline, relevant for this work.

In Fig. 2, we summarize the performance of our covariance matrix reconstruction pipeline across the two distinct samples of 30 QSOs. The left panel corresponds to the X-shooter sample, while the right panel corresponds to the SDSS (BOSS) sample. Here, the red curves correspond to the flux ratios (reconstructed ML profile divided by true, unattenuated flux) for each individual QSO in each sample. The black solid line corresponds to the median flux ratio obtained over the 30 QSOs in each sample. For both, we follow the reconstruction procedure outlined in Section 3.1.2.

Immediately from Fig. 2, it is evident that the flux ratios across both samples follow very similar behaviour, exemplified by the remarkably similar shape in the median flux ratios, albeit with the SDSS sample exhibiting a slightly larger offset. This highlights that the higher quality X-shooter spectra in comparison to the BOSS training set does not produce any additional source of systematic biases. Thus explaining why the degradation of the XQR-30 spectra did not alleviate the issue. Further, for both samples a clear dip is evident between 1215 and 1230 Å.[11] That is, our reconstruction pipeline consistently underestimates the shape of the reconstructed Lyα + N V line profile within this region by $\sim$10 per cent irrespective of the quality of the observed spectra being reconstructed. Thus, the problematic feature identified earlier is systematic to our reconstruction pipeline.

The origin of this behaviour is due to the modelling of the QSO flux within this specific wavelength region. Here, the QSO flux is the sum of three Gaussian components,[12] the sum of a broad and narrow component for Lyα and a single component for N V. Deviations in the predicted locations and profile shapes of these Gaussian components can produce this decrement in the QSO flux between Lyα and N V. For example, a larger predicted separation between the broad Lyα and N V lines caused by either (or both) a bluer than expected Lyα line centre or redward N V line centre or a narrower than expected width in these line profiles would produce a flux decrement within this spectral region. Owing to the notably lower strength of the N V emission line correlations (compared to the Lyα components) with the other emission lines in our covariance matrix (see e.g. Fig. A1) the N V is going to be less strongly constrained (i.e. larger uncertainty)

[10] Although some QSOs from our expanded training set likely exist in this sample of 30 BOSS QSOs, since our reconstruction method relies on drawing from a Normal distribution based on a covariance matrix of line properties our reconstructions will not be biased by their appearance.

[11] Note that this feature occurs over a different rest-frame wavelength range purely due to the blueshift of ATLAS J025 − 33 used in our previous example.

[12] Although in theory we could consider additional Gaussian components to improve the ability to fit the Lyα + N V line complex, the overall correlation strengths between additional (beyond two) Lyα components and the other high-ionization lines would diminish as additional components are not always required to fit the observed training data.

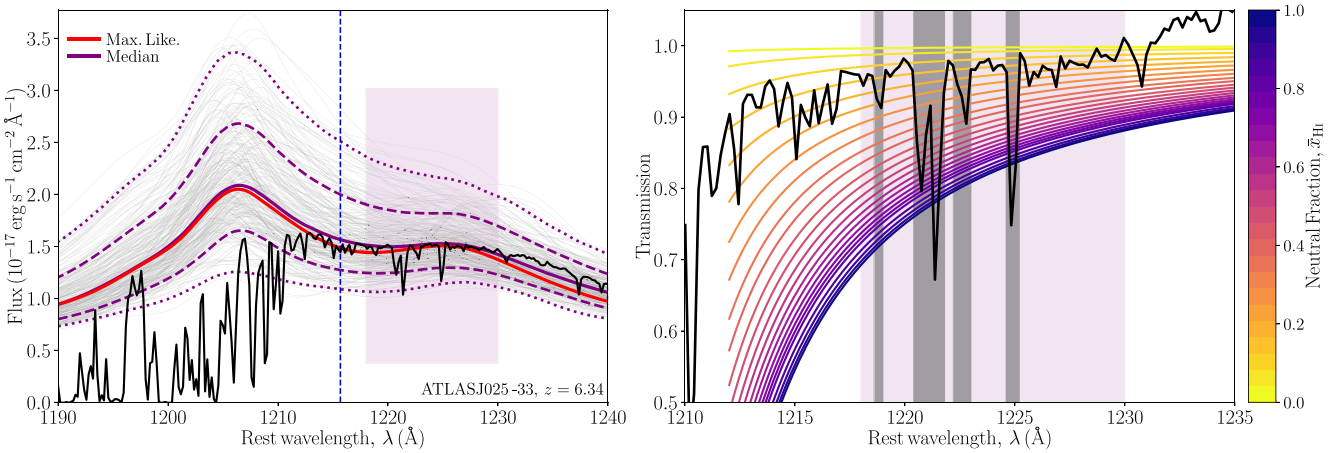

Figure 3. The same as Fig. 1 except after recalibrating our reconstruction pipeline using template spectra from two different QSO samples (see the text for further details).

and thus more likely to be the cause of the flux decrement than the broad Lyα component. Importantly, given that these components are sufficient for fitting QSOs within this spectral region (i.e. in our training set), it may also indicate that there are higher order correlations between our emission line parameters we are missing within our covariance matrix approach. In future, we aim to explore this further but for the purposes of this work, we will recalibrate our profiles to mitigate this feature.

It is worth pointing out that this feature was not identified in our previous study of $z > 7$ QSOs for several reasons. Other than for ULASJ1120 + 0641, there is no clear/prominent N v line in the data and further a very broad Lyα line is preferred. As a result, there was limited opportunity for this feature to manifest as it requires a notable N v line component. For ULASJ1120 + 0641, the relatively broad observed N v line profile extends sufficiently redward to benefit from our prior on the observed QSO flux. Therefore, this prior enables us to predict a relatively broad N v line component, limiting the potential impact of this feature. Thus, only with the exquisite quality of the X-shooter spectra coupled with the more prevalent N v line features has this feature become apparent.

It is important to note that this particular problem is intrinsic to our reconstruction method, as it relies upon the sum of three predicted Gaussian components to describe the Lyα + N v line complex. Other reconstruction pipelines in the literature provide flux predictions based off the sum of components following principal component analysis (PCA) or profiles drawn from machine learning approaches which are more agnostic to the direct emission line correlations (e.g. Davies et al. 2018b; Fathivavsari 2020; Reiman et al. 2020; Ďurovčíková et al. 2020; Bosman et al. 2021; Liu & Bordoloi 2021; Chen et al. 2022; Sun et al. 2023). As a result, these appear to be less susceptible to such systematic biases in the reconstructed profiles (see Greig et al. 2024, for more detailed discussions).

Crucially, and relevant for this work, the consistency of the flux ratios across the two samples implies that we should be able to recalibrate our reconstruction pipeline to correct for this systematic offset in our reconstruction profiles. To do so, we convolve each random draw from our covariance matrix reconstruction by the distribution of flux ratios shown in Fig. 2 (both from the X-shooter and SDSS sample). A consequence of this recalibration is that the distribution of reconstructed profiles will become broader, reflecting the increased scatter injected by sampling from these flux ratios and subsequently also broader uncertainties on the inferred IGM neutral fraction. Note, this convolution only occurs once we have corrected for the blueshift of the reconstructed QSO. That is, we shift these flux ratios to be centred on the location of the Lyα profile estimated from the reconstruction pipeline to ensure we are correctly recalibrating over the problematic region between Lyα and N v.

In Fig. 3, we demonstrate the performance of this recalibration on the QSO, ATLAS J025 − 33, (as shown in Fig. 1). In the left panel, we present our calibrated reconstruction and in the right panel, the corresponding Lyα transmission following this recalibration. Note, for the ML profile (red curve) we simply multiply it by the median flux ratio from Fig. 2 for visualization purposes. In the left panel, we can easily identify the two main aspects of this recalibration procedure. First, the shape of the median profile between 1210 and 1220 Å no longer possesses the parabolic dip observed in Fig. 1 (more readily visible in the right panel) and secondly, the broader distribution (and increased diversity) of the random profiles draws from our covariance matrix reconstruction. Note, that by performing our recalibration for this particular object, the predicted median flux is now below the observed spectrum at $\gtrsim 1230$ Å. However, this is not too concerning as it is at the redward edge of the N v line, whereas the purpose of the recalibration is to improve the reconstructions more so on the blue side of N v and the redward edge of Lyα (the joint contribution of the Lyα and N v line components). Nevertheless, this will be explored in greater detail in future work when working to improve on this QSO reconstruction method.

The right panel of Fig. 3 more readily demonstrates the improvements this recalibration brings to our reconstruction pipeline. Correcting this systematic offset in the shape of the reconstructed profiles produces corresponding Lyα transmission profiles which now better match the expected shape of the synthetic IGM damping wing profiles. That is, the observed Lyα transmission is now monotonically increasing with rest-frame wavelength, enabling more robust template matching against the synthetic sampling wing profiles drawn from the EoR simulations.

3.5 Joint fitting to obtain IGM neutral fraction constraints

We obtain our constraints on the IGM neutral fraction by jointly sampling our synthetic damping wing profiles from our EoR simulations convolved with our recalibrated intrinsic Lyα profile reconstructions. Our fitting pipeline is as follows:

(i) We draw $\sim 10^5$ intrinsic QSO profile estimates from the reconstructed Lyα and N V line profiles (see Section 3.1).

(ii) We convolve these $\sim 10^5$ reconstructed profiles by the blueshift corrected template flux ratios to recalibrate for a systematic $\sim$10 per cent underestimate of the intrinsic flux as outlined in Section 3.4 leading to $\sim 10^6$ corrected reconstruction profiles.

(iii) Each intrinsic profile is then multiplied by 10^5 synthetic damping wing opacities following Section 3.2. This results in $\sim 10^{11}$ mock spectra for each $\bar{x}_{\rm HI}$ snapshot from the EoR simulation.

(iv) Each $\sim 10^{11}$ mock spectra is then individually compared to the observed QSO spectrum over the $\lambda = 1218$–1230 Å region (consistent with Greig et al. 2017b; Greig et al. 2019; Greig et al. 2022). For each, we calculate a χ^2 relative to observed flux and the error spectrum. Where appropriate, absorption features or other problematic regions of the observed spectrum over this fitting range are masked out following visual inspection that could otherwise incorrectly bias our results.

(v) We then obtain a likelihood for the current $\bar{x}_{\rm HI}$ by averaging (marginalizing) over all $\sim 10^{11}$ mock spectra drawn from the corresponding $\bar{x}_{\rm HI}$ snapshot.

(vi) Steps (ii)–(v) are then repeated for all available $\bar{x}_{\rm HI}$ snapshots (24) to obtain a final 1D probability distribution function (PDF) of the $\bar{x}_{\rm HI}$ for our particular observed QSO.

Importantly, unlike in our previous works, in step (iv) we rebin the observed spectrum onto 1 Å bins over the entire $\lambda = 1218$–1230 Å region. Additionally, we were also required to enlarge the amplitude of the provided flux errors by a factor of 5.[13] These steps were necessitated owing to the considerably higher resolution and correspondingly small error spectrum provided by X-shooter. In the absence of this rebinning and enlarged errors, we found our simple analytic χ^2 estimate of the likelihood would encounter numerical difficulties owing to sampling large χ^2 values and correspondingly being too sensitive to narrow subsets of individual profiles who matched the observed data. Alternatively, we could have considered a narrow-wavelength range, however, doing so is more prone to biasing the results to particular features in the data. This highlights the necessity to improve our joint fitting pipeline which we will pursue in future work, where we will move away from using analytic likelihoods altogether in favour of likelihood-free or simulation-based inference (see e.g Cranmer, Brehmer & Louppe 2020, for a recent review on such methods and a preliminary exploration of simulation based inference for extracting constraints from QSO damping wings by Chen, Speagle & Rogers 2023).

4 RESULTS

4.1 Reconstruction of the XQR-30 sample

In Fig. 4, we provide the reconstructed intrinsic profiles for the 23 QSOs from the XQR-30 sample deemed suitable for IGM damping wing analysis (see Section 2.2). In each panel, we show the ML reconstruction profile (red curve), 300 random draws from our full posterior distribution (thin grey lines), the median (solid purple curve), and 68th (purple dashed) and 95th (purple dotted) percentile profiles obtained from the full posterior distribution. The purple-shaded box corresponds to the 1218–1230 Å region over which we fit for the damping wing imprint. In the inset panel, we provide the Lyα transmission profile over this 1218–1230 Å region obtained using the median profile, highlighting the presence (if any) of an IGM damping wing imprint. Grey-shaded regions correspond to features removed from our likelihood fitting.

Here, we will limit our discussions of these reconstructed QSOs to focus only on broad observations that can be made across the sample, and only focus on individual QSOs that warrant further discussion. First, for the most part, the Lyα transmission profile within the 1218–1230 Å region either appears flat, consistent with little to no IGM attenuation, or monotonically increasing with rest-frame wavelength. This indicates that our recalibration step to our reconstruction pipeline is performing well in mitigating our observed systematic offset in the predicted intrinsic flux between the Lyα and N V emission lines (see Sections 3.3 and 3.4).

However, potentially problematic QSO reconstructions remain, for example in the case of J060 + 24 and J359 − 06, which exhibit smoothly varying features in their transmission profiles. For the latter, this behaviour should not impact the results as the relative change in amplitude of the transmission profile is fairly modest. For the former, the shape appears to be driven more so by a stronger blueshift in the Lyα line profile leading to the uptick in transmission near 1218 Å. As a result this may result in a slight underestimate of the neutral fraction. ATLASJ029 − 36, VDESJ0224 − 47, and J1509 − 1749 also may exhibit similar features to those above but to a notably lesser extent. However, what is important is that since we draw from the full posterior distribution of reconstructed profiles that are convolved with the synthetic damping wing templates, profiles that better match the observed spectrum should result in a higher likelihood and thus dominate the constraining power. That is, using the full distribution of joint fits will be a better match than the median transmission profile that is provided for visualization purposes only.

4.2 Recovered IGM damping wing constraints

In Fig. 5, we present the marginalized 1D PDFs of the IGM neutral fraction for each of the 23 QSOs of the XQR-30 sample. For this, we separate the QSOs into redshift bins of $\Delta z = 0.1$. In each panel, the thin coloured lines correspond to an individual QSO. For the vast majority of QSOs in the sample we recover broad, one-sided distributions, consistent with no IGM attenuation. This, however, is not too surprising given the relatively small decrement in the Lyα transmission profiles shown in the inset panels of Fig. 4. Nevertheless, we still find several QSOs with marginalized 1D PDFs consistent with a detection of IGM attenuation.

We summarize the individual constraints/limits on the IGM neutral fraction from the XQR-30 sample in the fourth column of Table 1. For marginalized 1D PDFs consistent with a detection, we present the median and 68th percentiles of the posteriors. For the 1D PDFs consistent with no attenuation, we present the 68th percentile upper limits, which is the IGM neutral fraction which encloses 68 per cent of the total probability.

In the left panel of Fig. 6, we plot our individual QSO constraints on the IGM neutral fraction as a function of redshift. In Table 2, we summarize our joint constraints on the IGM neutral fraction after binning in redshift. In the right panel of Fig. 6, we provide the violin plots of the IGM neutral fraction after binning our individual QSOs into separate $\Delta z = 0.1$ redshift bins based loosely on the natural redshift sampling of the available QSOs in the XQR-30 sample. This choice of redshift sampling is fairly arbitrary but is adopted to ensure each bin contains multiple QSOs. We explored several alternative choices in binning (i.e. larger), but found the results to be generally

[13] We explored increasing this error by factors of 2, 5, and 10 and found no discernible difference in the inferred constraints other than a broadened PDF for increasing error. Thus we chose a factor of two to limit the amplitude of the increased error spectrum.

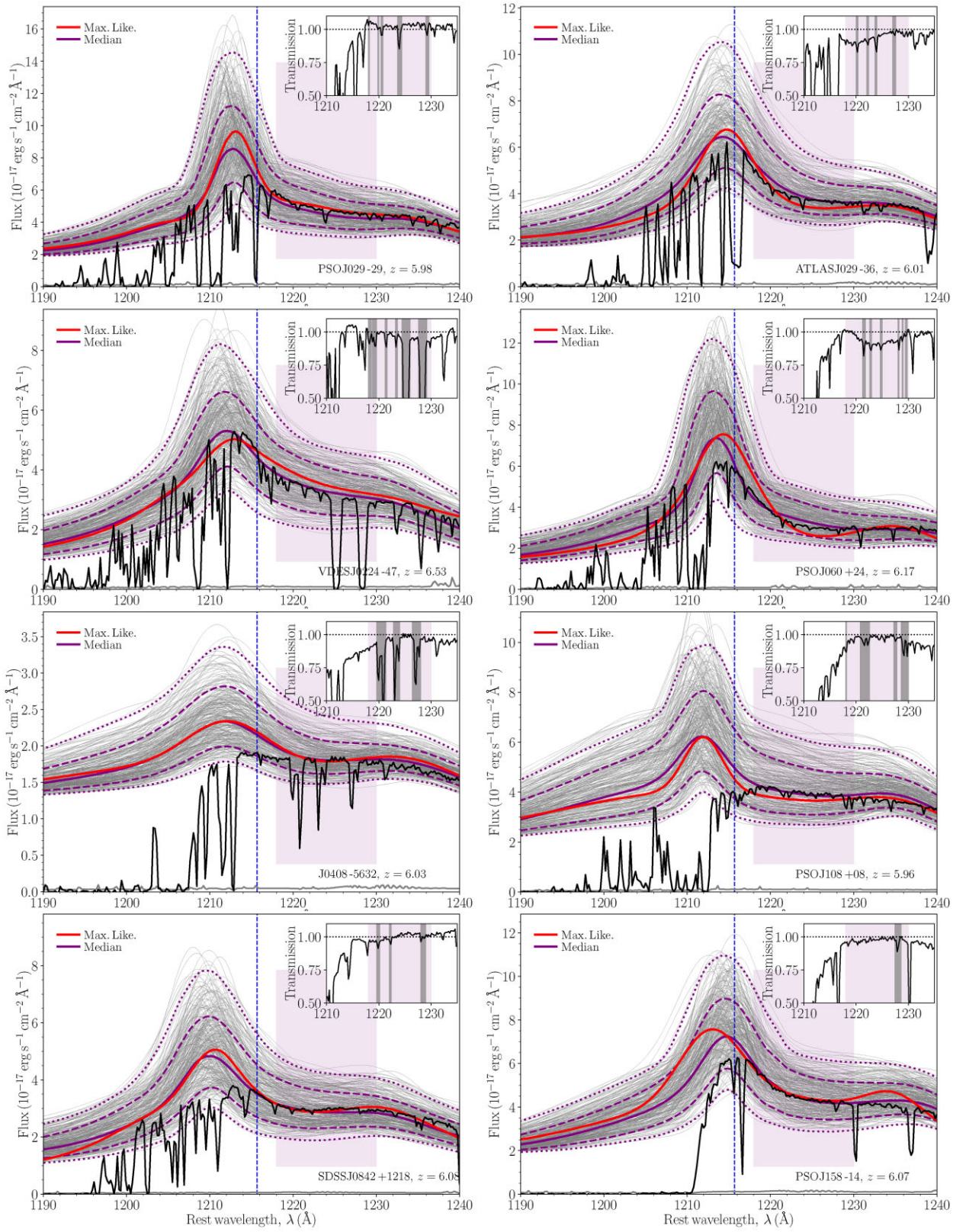

Figure 4. Intrinsic QSO reconstructions of the XQR-30 sample. We provide the ML reconstruction (red curve), the purple solid, dashed, and dotted curves correspond to the median, 68th and 95th percentile profiles and the thin grey curves represent 300 random draws from our full posterior distribution. The solid thick grey curve near zero corresponds to the QSO noise spectrum, amplified by a factor of 5 to improve the numerical performance of our neutral fraction inference approach (see the text for further details). The purple-shaded box demarcates our damping wing fitting region (1218–1230 Å region). Inset panel: the Lyα transmission profile highlighting the presence (if any) of an IGM damping wing imprint (i.e. observed transmission spectrum below unity) assuming the median (purple curve). Grey-shaded regions correspond to features in the observed spectrum removed from our likelihood fitting.

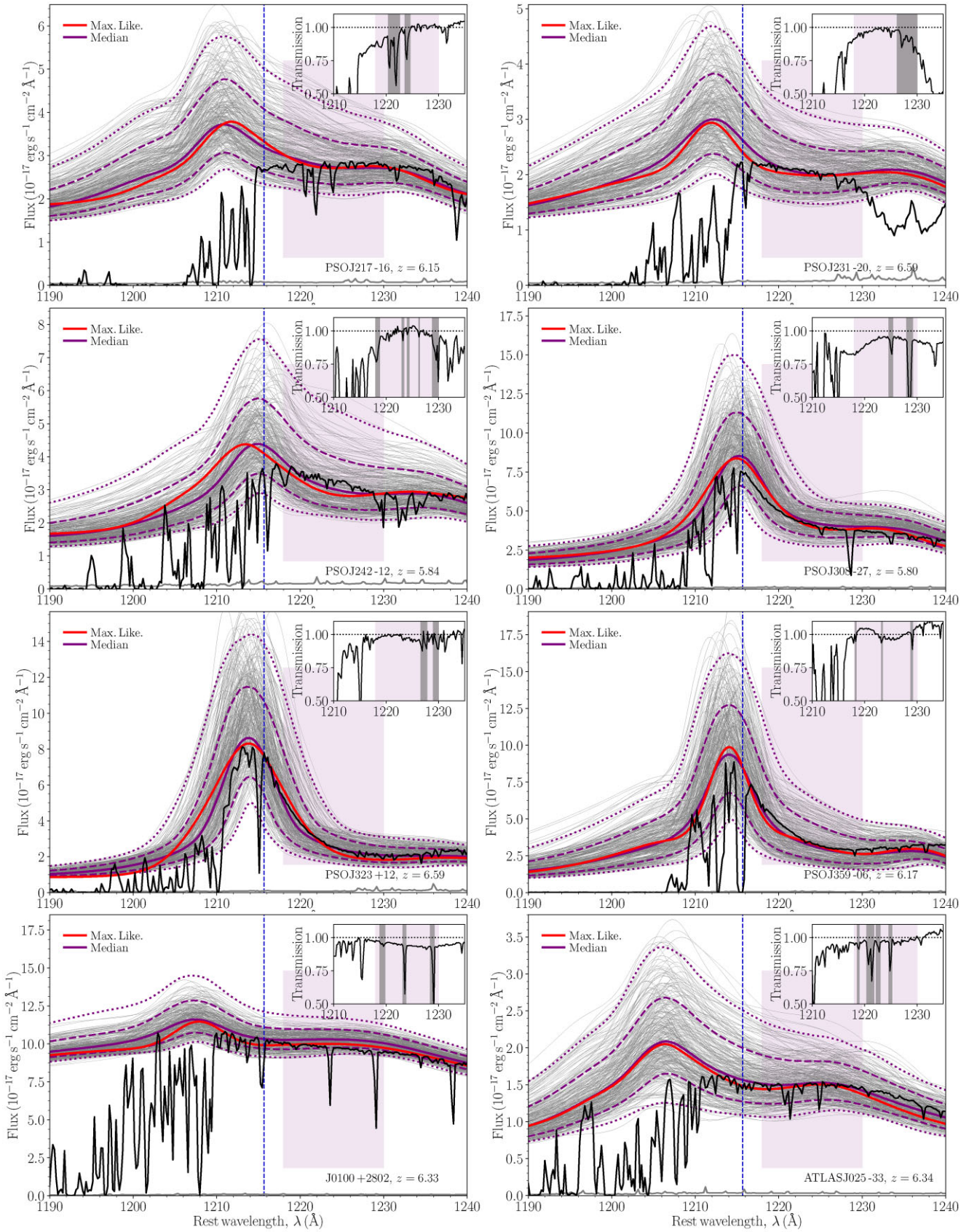

Figure 4. *Continued.*

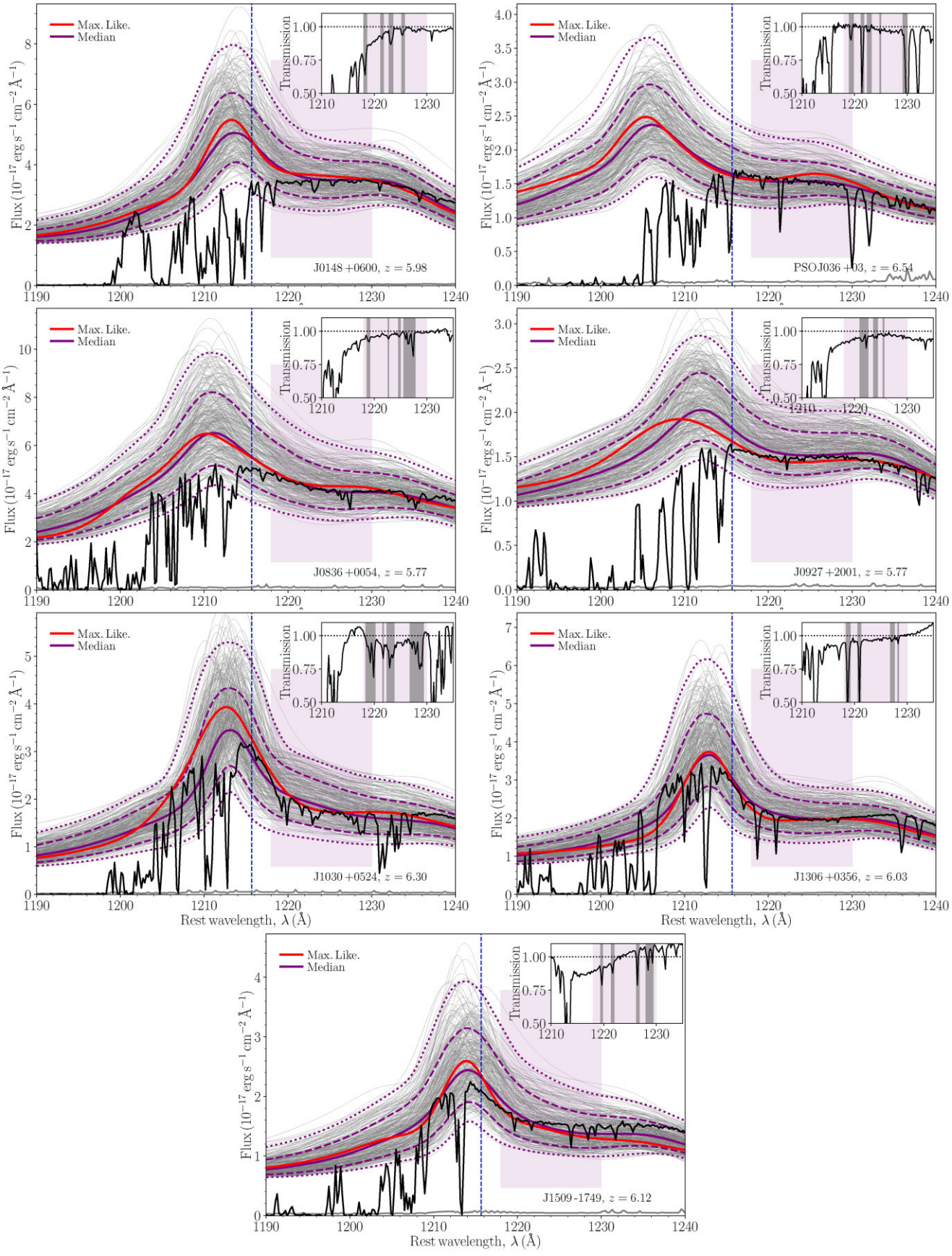

Figure 4. *Continued.*

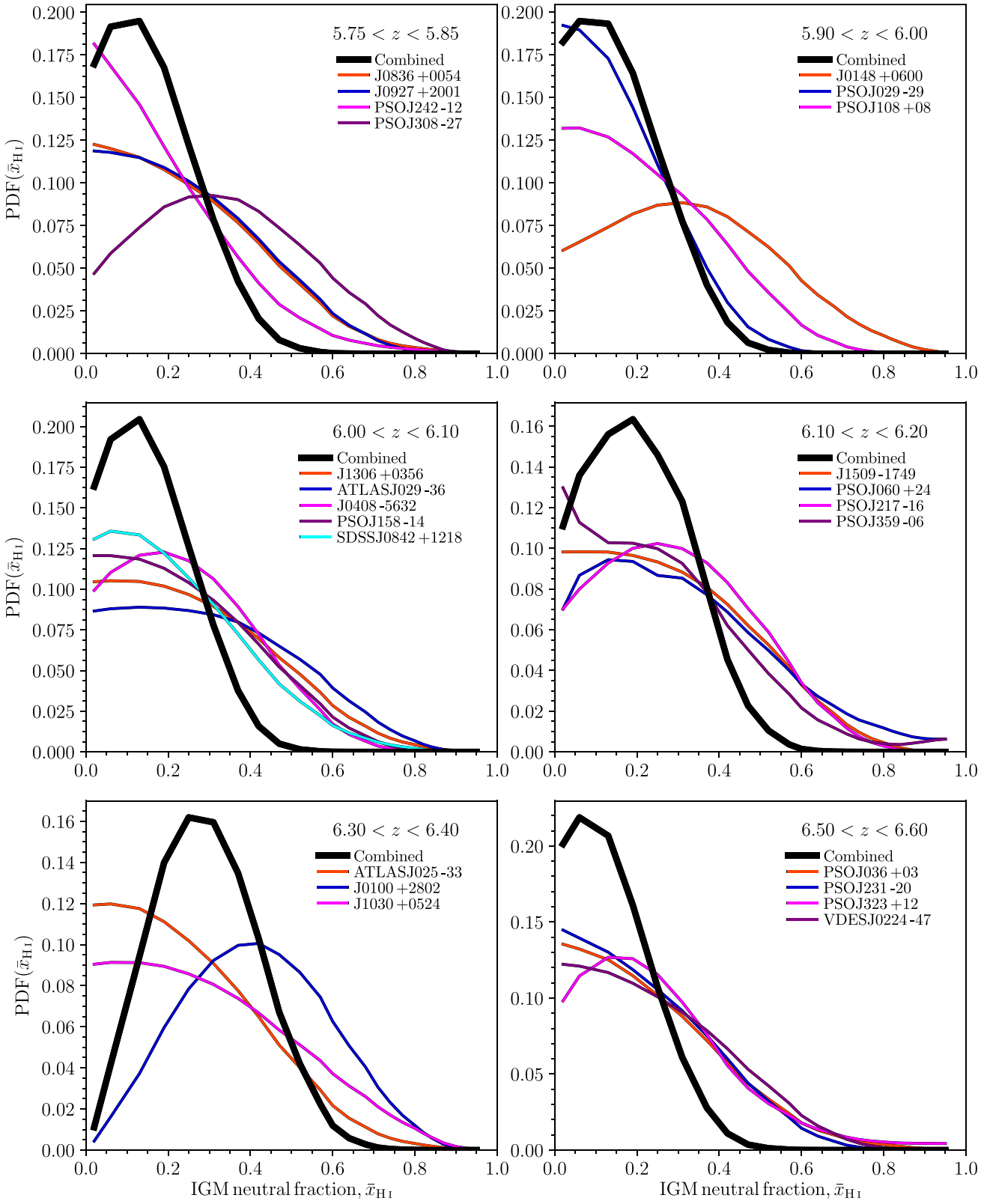

Figure 5. The marginalized 1D PDFs of the IGM neutral fraction for each of the XQR-30 QSOs, separated into redshift bins of $\Delta z = 0.1$. The thin coloured curves in each panel correspond to the recovered constraints for individual QSOs, whereas the thick black curve corresponds to the bin-averaged constraint on the IGM neutral fraction.

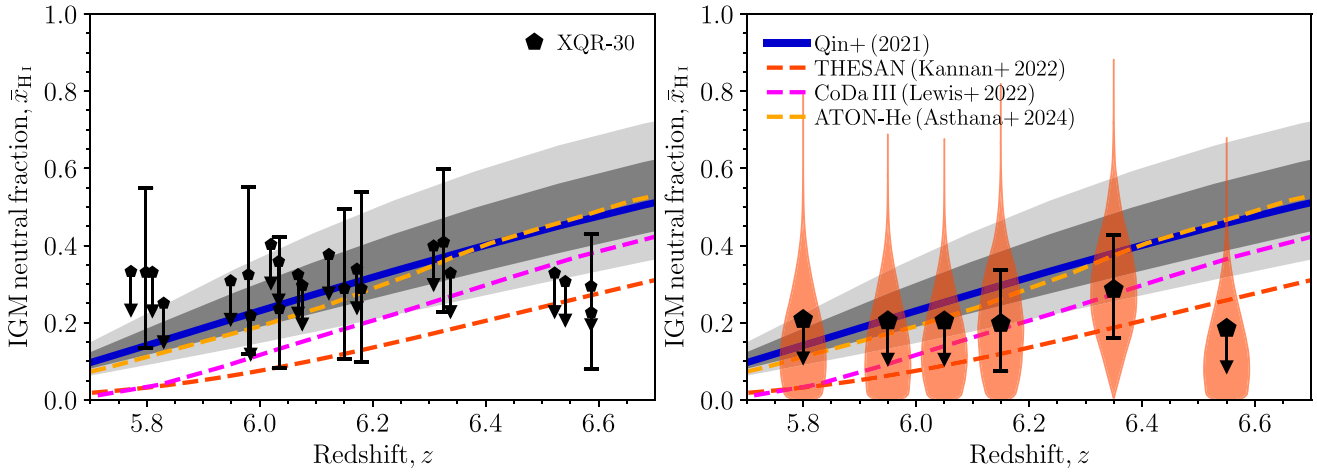

Figure 6. Our constraints on the IGM neutral fraction following our damping wing analysis of the XQR-30 sample. Left panel: the individual constraints on the IGM neutral fraction. We present the median and 68th percentiles for our constraints and 68th percentile upper limits for QSOs consistent with no IGM attenuation. Right panel: a violin plot demonstrating the constraints on the IGM neutral fraction after binning our QSOs into $\Delta z = 0.1$ redshift bins (whereby the individually recovered PDFs of all QSOs within each redshift bin are multiplied to obtain an averaged constraint). In both panels, the blue curve and the dark- and light-shaded regions correspond to the median, 68th and 95th percentile EoR histories obtained by Qin et al. (2021, see the text for further details). Further, the dashed red, magenta, and orange curves correspond to the fiducial reionization histories of state-of-the-art numerical simulations of the IGM from THESAN (Garaldi et al. 2022; Kannan et al. 2022), and CoDA III (Lewis et al. 2022) and Asthana et al. (2024).

Table 2. Summary of the redshift binned IGM neutral fraction constraints from our damping wing analysis. For IGM neutral fractions posteriors consistent with a detection, we provide the median and 68th percentiles. Remaining constraints are presented as 68th percentile upper limits.

Redshift range	$\bar{x}_{\rm H\,I}$	QSOs in bin
$5.85 \leq z < 5.95$	<0.21	4
$5.90 \leq z < 6.00$	<0.20	3
$6.00 \leq z < 6.10$	<0.21	5
$6.10 \leq z < 6.20$	$0.20^{+0.14}_{-0.12}$	4
$6.30 \leq z < 6.40$	$0.29^{+0.14}_{-0.13}$	3
$6.50 \leq z < 6.60$	<0.18	4

insensitive to the choice owing to the natural redshift sampling of the data.

In both panels, we also provide the constrained EoR histories from the state-of-the-art Monte-Carlo Markov Chain analysis of Qin et al. (2021). Here, these authors ran seminumerical simulations of the 21-cm signal during the EoR using 21CMFAST (Mesinger & Furlanetto 2007; Mesinger, Furlanetto & Cen 2011; Murray et al. 2020) coupled with a hybrid scheme to model the Lyα forest. Using these simulations, their astrophysical model describing the galaxies responsible for reionization are constrained only against existing observational constraints on the reionization epoch such as; the observed UV galaxy LFs at $z = 6$–10, the electron scattering optical depth, $\tau_{\rm e}$, measured by *Planck* (Planck Collaboration VI 2020), the dark pixel limits on the IGM neutral fraction (McGreer et al. 2015) and PDFs of the Lyα effective optical depth from the Lyα forest at $z =$ 5–6 (Bosman et al. 2018). Post-processing of the resultant posteriors on their inferred astrophysical model then yields a posterior on the allowed reionization history given the existing observational data. We overlay the median (blue curve) and the 68th (dark grey) and 95th (light grey) percentile regions of the constrained EoR histories.

The vast majority of our inferred IGM damping wing constraints from the XQR-30 sample strongly align with the inferred EoR histories from Qin et al. (2021). Further, in general our XQR-30 data points monotonically increase in IGM neutral fraction for increasing redshift, consistent with ongoing reionization. The main discrepancy with our results and those from Qin et al. (2021) are the inferred IGM neutral fraction limits at $z \gtrsim 6.5$. Our IGM damping wing limits at $z \gtrsim 6.5$ are systematically below the inferred EoR histories from Qin et al. (2021). Our one constraint within this bin, PSOJ323 + 12, returns an IGM neutral fraction of $\bar{x}_{\rm H\,I} = 0.23^{+0.19}_{-0.15}$, which owing to the broad 68th percentiles is consistent with the inferred EoR history. For the remaining three QSOs, we recover upper limits at $z \gtrsim 6.5$ that are inconsistant at between 68th and 95th percentiles of the joint distribution. In Appendix B, we explored the role of the assumed prior on our minimum H II bubble size, $R_{\rm min}$. For our available four choices of $R_{\rm min}$, we observe a shift of $\sim$0.02 in the inferred IGM neutral fraction from our lowest to highest choice of $R_{\rm min}$ therefore our adopted choice of averaging over $R_{\rm min}$ is not likely a contributing factor to the lower IGM neutral fractions. Within the literature there are a broad range of approaches to both extract the damping wing imprint and to predict the intrinsic QSO profile, thus it would be prudent to perform a re-analyses of these QSOs using these alternative reconstruction/damping wing fitting pipelines to add further confidence to the results presented in this work. However, this is a significant undertaking and we leave such a re-analysis to future work.

To place these constraints into a broader context, we additionally provide the reionization histories from recent state-of-the-art radiation-hydrodynamic simulations from THESAN (Garaldi et al. 2022; Kannan et al. 2022) and Cosmic Dawn III (CoDa III, Lewis et al. 2022). We also provide the reionization history from Asthana et al. (2024) who post-processed the Sherwood simulation suite (Bolton et al. 2017) using radiative transfer. Note that unlike the Qin et al. (2021) posteriors, which are constrained specifically by the Bosman et al. (2018) Lyα forest data, the THESAN and CoDA III simulations are single simulations designed to match a considerably broader range of existing observational data. As a result, their reionization histories will differ to those from Qin et al. (2021). On the other hand, the Asthana et al. (2024) simulations are specifically designed to match the XQR-30 Lyα forest data of Bosman et al.

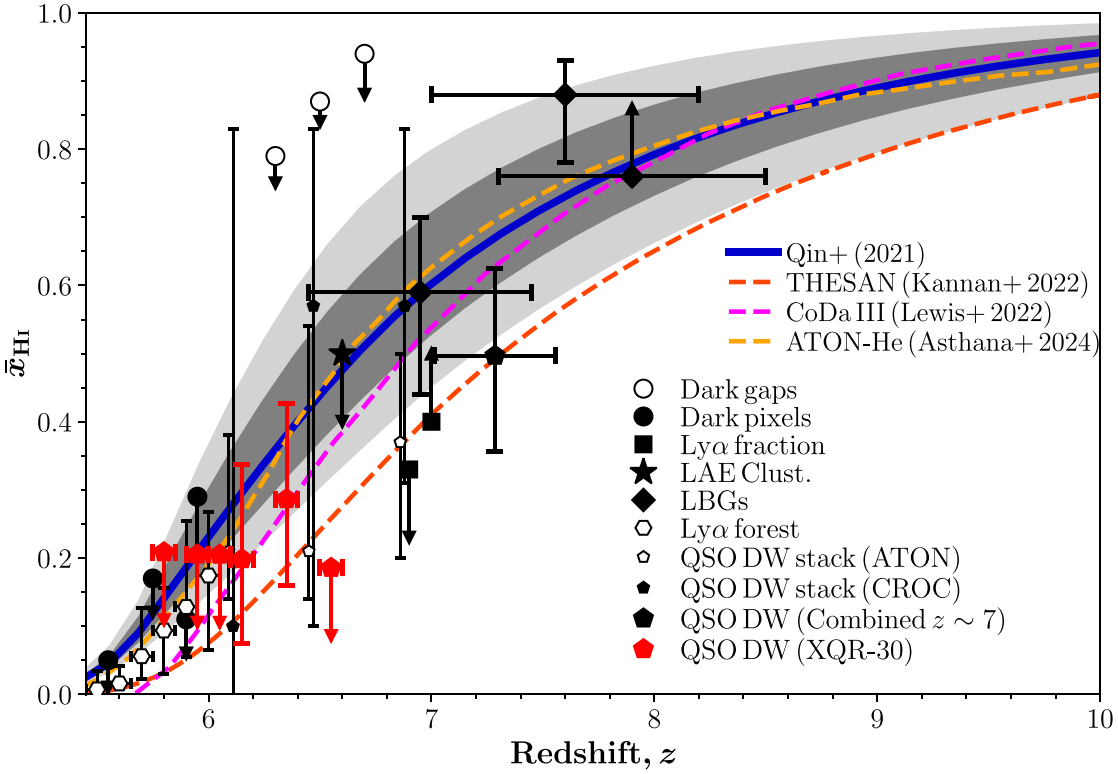

Figure 7. Our binned IGM neutral fraction constraints as a function of redshift in the context of other EoR observables. Red pentagons: the XQR-30 sample (this work). Large black pentagon: the combined IGM damping wing constraints of all 4 $z > 7$ QSOs (Greig et al. 2022). Small pentagons: IGM damping wing constraints from stacking QSO reconstruction profiles (Ďurovčíková et al. 2024). Open hexagon: the inferred constraints from the Lyα forest using numerical simulations at $z = 5.5$–6.0 (Gaikwad et al. 2023). Open circles: dark gaps at $z = 6.3$, 6.5, and 6.7 (Zhu et al. 2022, obtained with XQR-30). Circles: dark pixels at $z = 5.9$ (McGreer, Mesinger & D'Odorico 2015) and $z = 5.55$, 5.75, and 5.95 (Jin et al. 2023). Squares: the Lyα fraction at $z = 6.9$ (Wold et al. 2022) and $z = 7$ (Mesinger et al. 2015), stars: LAE clustering at $z = 6.6$ (Sobacchi & Mesinger 2015), diamonds: LBGs at $z = 7$ (Mason et al. 2018), $z = 7.6$ (Hoag et al. 2019), and $z = 8$ (Mason et al. 2019). The blue curve and the dark- and light-shaded regions corresponds to the median, 1σ and 2σ constraints from (Qin et al. 2021, see the text for further details) and the dashed red, magenta, and orange curves correspond to the fiducial reionization histories of state-of-the-art numerical simulations of the IGM from THESAN (Garaldi et al. 2022; Kannan et al. 2022), and CoDA III (Lewis et al. 2022) and Asthana et al. (2024).

(2022) and as such the reionization history is very similar to the median history recovered by Qin et al. (2021).

Our individual inferred IGM damping wing constraints form the XQR-30 sample remain broadly consistent with the reionization histories from these state-of-the-art numerical simulations. Although the THESAN and CoDa III reionization histories are $\Delta\bar{x}_{\rm HI} \sim 0.1 - 0.15$ lower than that expected explicitly from the Lyα forest, since the vast majority of our results are only upper limits these remain statistically consistent. For the handful of constraints that we recover, the CoDa III simulation is consistent with all but one constraint at $z \sim 5.8$ whereas the THESAN simulations are inconsistent with several of our constraints. However, as noted above these simulations are not explicitly constrained to match the Lyα forest data, but instead to broadly match a large range of existing observations. Thus, any inconsistencies are not too concerning. Importantly, at $z \gtrsim 6.5$ where our XQR-30 damping wing results begin to disagree with the inferred constraints from the Lyα forest data, the THESAN and CoDA III simulations are perfectly consistent within the 68th percentile uncertainties of our constraints and upper limits. Therefore, the stronger inconsistencies with our damping wing results and the inferred constraints on the reionization history using the Lyα forest data at $z \sim 6.5$ can likely be softened once additional observational constraints are folded into such an analysis. Nevertheless, once we bin the individual constraints (right panel of Fig. 6) our inferred limits at $z \gtrsim 6.5$ are still inconsistent at more than the 68th percentiles with all these numerical simulations.

4.3 Compilation of reionization constraints

To place our constraints in a broader reionization context, in Fig. 7 we compare our binned IGM neutral fraction constraints against a compilation of other existing constraints on the IGM neutral fraction. Here, we consider constraints and limits obtained from: (i) dark gaps (Zhu et al. 2022) (ii) dark pixels (McGreer et al. 2015; Jin et al. 2023), (iii) the Lyα fraction at $z = 6.9$ (Wold et al. 2022) and at $z = 7$ (Mesinger et al. 2015), (iv) the clustering of Lyα emitters (LAEs) at $z = 6.6$ (Sobacchi & Mesinger 2015), (v) Lyman-break galaxies (LBGs) at $z = 7$ (Mason et al. 2018), $z = 7.6$ (Hoag et al. 2019) and at $z = 8$ (Mason et al. 2019), (vi) the inferred constraints comparing numerical simulations to the Lyα forest at $z = 5.5$–6.0 (Gaikwad et al. 2023), (vii) the joint QSO IGM damping constraint combining all 4 $z > 7$ QSOs (Greig et al. 2022), and (viii) IGM damping constraints after stacking continuum normalized QSO spectra (Ďurovčíková et al. 2024). Note, this is not intended to be an exhaustive list, but instead provide a broad selection of approaches and redshift ranges. We also include the reionization histories of the various state-of-the-art numerical simulations as introduced previously.

Our constraints on the IGM neutral fraction after binning in redshift intervals of $\Delta z = 0.1$ remain consistent with existing constraints on the EoR in the literature. Except for our limit at $z \sim 6.5$, which is now inconsistent at more than 95 per cent. However, it is consistent with the recent QSO damping wing analysis of Ďurovčíková et al. (2024), although their posteriors are extremely broad owing to the parameter space binning of their simulations. The reason for our increased inconsistency is due to the multiplication of the individual posteriors within this redshift bin. Since three of the four QSOs are consistent with no IGM attenuation, the multiplication of these strengthens the preference for a posterior consistent with no IGM attenuation. In order to confirm the results of this work, independent re-analysis of the XQR-30 sample using alternative reconstruction and/or damping wing fitting are required.

4.4 Discussion

It is important to point out that the IGM damping wing constraints presented in this work use only a single QSO reconstruction methodology (covariance matrix). As highlighted previously, there are numerous approaches throughout the literature based on different underlying assumptions. For example, rather than explicitly using the correlations amongst emission lines to reconstruct the intrinsic flux, one can instead use correlations amongst the PCA components (e.g. Davies et al. 2018b; Bosman et al. 2021; Chen et al. 2022). Instead of directly mapping these correlations one can learn them via neural networks (Ďurovčíková et al. 2020) or deep learning (Liu & Bordoloi 2021) and project the reconstruction uncertainties using normalizing flows (Reiman et al. 2020). Alternatively, one can use factor analysis to produce a more flexible basis set of components rather than those from PCA (Sun et al. 2023). Finally, one can also perform deep learning to predict the QSO flux per pixel based on a training set of QSOs (Fathivavsari 2020).

In Greig et al. (2024), we perform a detailed comparison of these reconstruction pipelines on a unified set of QSOs from two separate instruments (X-shooter and SDSS). Qualitatively speaking, these reconstruction pipelines tend to be consistent with one another within their associated modelling uncertainties. However, quantitatively, there can be some notable differences from object to object and these differences would filter through to attempts to recover constraints on the IGM neutral fraction through the damping wing. In the case of this data set, with the high-quality X-shooter spectra, these numerical differences in the predicted QSO profiles could result in considerable differences in the inferred IGM neutral fractions from various reconstruction pipelines.

Not limited to just the reconstruction method, but the methodology to infer the IGM damping wing signature also differs in the literature. Here, we restrict our approach to fitting the smoothed IGM imprint using large-volume EoR simulations to generate synthetic damping wing profiles in the range $\lambda = 1218$–1230 Å. Our choice is based on a preference to avoid having to model and marginalize over the uncertainties of the host QSO environment. In taking into account the QSO host environment, one can better deal with uncertainties in the QSO lifetime and affords a larger region over which to search for the damping wing imprint (e.g. $\lambda \sim 1190$–1230 Å in Davies et al. 2018b). Alternatively, one can simply use an analytic model of the red damping wing imprint (Miralda-Escudé 1998) in order to gain an estimate of the IGM neutral fraction (e.g. Bañados et al. 2018; Reiman et al. 2020).

All of the approaches mentioned previously have their own underlying assumptions and uncertainties. Therefore, to be able to obtain robust estimates of the IGM neutral fraction from the smooth imprint of the IGM damping wing, realistically, one could average (marginalize) over the vast array of different approaches in the literature. In doing so, one would average over the differences in methodology and thus the various systematics and uncertainties. At the very least, independent confirmation using any of the existing other methods would add credence to our recovered constraints.

Another important point worth reiterating is that to be able to obtain our IGM damping wing constraints we had to (i) recalibrate our reconstruction profile and (ii) degrade the observed X-shooter spectra. In the case of the former, this implies further improvements are necessary to our reconstruction pipeline to robustly account for the predicted Lyα and N V line profiles. In the case of the latter, we rebinned the spectra onto 1 Å bins and further had to increase the associated error in the spectra owing to the inflexibility of the analytic (χ^2) expression used in our joint likelihood fitting. In addition to it being inflexible, it also does not fully take advantage of covariances in the observational data. Presently, the observed flux in each wavelength bin is take to be an independent measurement, ignoring the known correlations with neighbouring bins. In fact, we use these correlations to predict our reconstructed profiles (Gaussian components). Given the wealth of theoretical data at hand, one could employ a form of simulation based inference (see e.g Cranmer et al. 2020, for a recent review) to learn the likelihood that more directly connects our reconstructed QSO profiles to the underlying IGM neutral fraction of our synthetic damping wing profiles (see e.g. Chen et al. 2023, for a preliminary demonstration).

Recently there have also been observations of Lyα emission from galaxies extending into the EoR (e.g. Endsley & Stark 2022; Jung et al. 2022; Hayes & Scarlata 2023; Saxena et al. 2023; Umeda et al. 2023; Whitler et al. 2024; Witstok et al. 2024). Although galaxies are much fainter than QSOs, in principle a similar analysis can be performed to attempt to infer the presence of a Lyα damping wing in the individual galaxy spectra (see e.g. Keating et al. 2023). However, this is extremely difficult as the local interstellar medium and H I in the local circumgalactic medium make it much more challenging to infer the unabsorbed emission compared to that of QSOs. Improving the S/N or reducing the galaxy to galaxy variance through stacking (e.g. Umeda et al. 2023) is fundamentally limited by the fact that the damping wing imprint is non-linear and cannot be described by a mean profile convolved with a mean galaxy spectral energy distribution (i.e. the average of a product is not the same as the product of averages).

5 CONCLUSION

We performed an IGM damping wing analysis on the enlarged XQR-30 sample, consisting of 42 high-quality X-shooter spectra spanning $5.8 \lesssim z \lesssim 6.6$. Following careful selection cuts removing QSOs demonstrating BAL features or possible pDLA absorption systems along the line of sight, we are left with 23 of the original 42 QSOs for our IGM damping wing analysis. Nevertheless, this is a factor of 5 improvement over the number of individual QSOs that have been explored for signs of IGM damping wing attenuation due to ongoing reionization.

Our IGM damping wing analysis utilizes a covariance matrix reconstruction approach to predict the intrinsic QSO profile near Lyα (Greig et al. 2017b). The fundamental assumption of this approach is that emission lines can be accurately modelled as Gaussian profiles and that the Lyα and N V emission lines can be reconstructed from a covariance matrix of their correlations with other high-ionization emission lines. These lines, observed redward of Lyα (e.g. C IV, Si IV + O IV], and C III]), are easily measurable and unaffected

by IGM attenuation or other line-of-sight contamination. In our approach we fit the observed QSO spectrum over $\lambda = 1275$–2300 Å and draw reconstructed profiles spanning $\lambda = 1180$–1260 Å from our resultant marginalized covariance matrix describing the properties of Lyα and N V.

In the process of analysing the XQR-30 sample, we identified a systematic offset in the predicted QSO flux between rest-frame Lyα and N V owing to our methodology of modelling emission lines as Gaussian profiles. Within this region, slight differences between the wavelength separation or in the widths of either the broad component of Lyα or N V can result in a very modest flux decrement. Using two distinct samples of QSOs from X-shooter and SDSS between $3.5 < z < 4.5$ (unaffected by IGM attenuation), we quantitatively explored whether this was specific to the higher quality X-shooter spectra, or a general feature of our pipeline. We found a consistent median flux decrement of $\sim$10 per cent across both samples, indicative of it being intrinsic to our reconstruction pipeline. Importantly, the consistency in the shape and amplitude of this flux decrement allowed us to recalibrate our covariance matrix reconstruction pipeline by drawing from templates of our original reconstructions compared to the known truth (unattenuated QSO spectrum).

After recalibrating our reconstructed QSO profiles we jointly sample these with synthetic IGM damping wing profiles drawn from large volume EoR simulations (1.6 Gpc on a side with an EoR morphology driven by galaxies residing in $M_h \gtrsim 10^9\,\mathrm{M}_\odot$ haloes). Within our Bayesian framework we fit our reconstructed QSOs profiles multiplied by the synthetic IGM damping wing profiles against the observed QSO spectra of the XQR-30 sample. Specifically, we fit for the smooth component of the IGM damping wing imprint only redward of Lyα ($\lambda = 1218$–1230 Å). Following this pipeline, we recover 1D marginalized posteriors on the IGM neutral fraction from each individual QSO spectrum.

Across the available sample of 23 high-z QSOs, we find 7 with constraints on the IGM neutral fraction during the EoR while for the remaining 16 we recover upper limits. Making use of the large number of QSOs at our disposal, we binned our results in redshift intervals of $\Delta z = 0.1$. Following this, we obtain our final results on the IGM neutral fraction (median and 68th percentiles) during the tail end of reionization of $0.20^{+0.14}_{-0.12}$ and $0.29^{+0.14}_{-0.13}$ at $z = 6.15$ and 6.35. Further, we report 68th percentile upper-limits on the IGM neutral fraction of $\bar{x}_{\rm H\,I} < 0.21$, 0.20, 0.21, and 0.18 at $z = 5.8$, 5.95, 6.05, and 6.55.

These constraints on the IGM neutral fraction are consistent with those obtained from alternative methods in the literature. In particular, all but one of our constraints are within the joint 68th percentile constraints on the IGM neutral fraction obtained by the state-of-the-art forward modelling of recent Lyα forest data by Qin et al. (2021). The only discrepancy occurs in the highest redshift bin, $6.5 \leq z < 6.6$, which is inconsistent at 95 per cent certainty. Of the four QSOs from the XQR-30 sample in this redshift range, three are best modelled by upper limits consistent with no IGM attenuation. The fourth (PSOJ323 + 12) indicates an IGM neutral fraction of $\bar{x}_{\rm H\,I} = 0.23^{+0.19}_{-0.15}$. Taken at face value this implies that these 4 QSOs may reside in a patch of the Universe that was reionized earlier. We also explored whether our choice of averaging over the adopted minimum local H II bubble size, $R_{\rm min}$ containing the QSO plus galaxy contribution impacted these results. We found that increasing $R_{\rm min}$ had a fairly modest impact on the inferred value of $\bar{x}_{\rm H\,I}$, smaller than the corresponding 68th percentile uncertainties. Given the broad range of approaches in the literature designed to reconstruct the intrinsic properties of high-z QSOs, along with differing methodologies for extracting the IGM damping wing imprint, it would be valuable to repeat this analysis across multiple methods, averaging over the different pipeline systematics and uncertainties.

ACKNOWLEDGEMENTS

We would like to thank the anonymous referees whose comments improved this manuscript. Parts of this research were supported by the Australian Research Council Centre of Excellence for All Sky Astrophysics in 3 Dimensions (ASTRO 3D), through project no. CE170100013. AM acknowledges support from the Ministry of Universities and Research (MUR) through the PRIN project 'Optimal inference from radio images of the epoch of reionization' as well as the PNRR project 'Centro Nazionale di Ricerca in High Performance Computing, Big Data e Quantum Computing'. GDB was supported by the National Science Foundation (NSF) through grant AST-1751404. SEIB is supported by the Deutsche Forschungsgemeinschaft (DFG) under Emmy Noether grant no. BO 5771/1-1. HC thanks the support by the Natural Sciences and Engineering Research Council of Canada (NSERC), funding reference no. DIS-2022-568580. MGH has been supported by STFC grants ST/N000927/1 and ST/Y004191/1. YZ was supported by the NSF through award SOSPADA-029 from the NRAO. This work was performed on the OzSTAR national facility at Swinburne University of Technology. The OzSTAR program receives funding in part from the Astronomy National Collaborative Research Infrastructure Strategy (NCRIS) allocation provided by the Australian Government, and from the Victorian Higher Education State Investment Fund (VHESIF) provided by the Victorian Government. Based on observations collected at the European Southern Observatory under ESO programmes: 60.A-9024, 084.A-0360, 084.A-0390, 085.A-0299, 086.A-0162, 086.A-0574, 088.A-0897, 091.C-0934, 294.A-5031, 096.A-0095, 096.A-0418, 097.B-1070, 098.B-0537, 0100.A-0625, 0101.B-0272, 0102.A-0154, 1103.A-0817.

Funding for the Sloan Digital Sky Survey IV has been provided by the Alfred P. Sloan Foundation, the U.S. Department of Energy Office of Science, and the Participating Institutions. SDSS acknowledges support and resources from the Center for High-Performance Computing at the University of Utah. The SDSS web site is www.sdss4.org.

SDSS is managed by the Astrophysical Research Consortium for the Participating Institutions of the SDSS Collaboration including the Brazilian Participation Group, the Carnegie Institution for Science, Carnegie Mellon University, Center for Astrophysics | Harvard & Smithsonian (CfA), the Chilean Participation Group, the French Participation Group, Instituto de Astrofísica de Canarias, The Johns Hopkins University, Kavli Institute for the Physics and Mathematics of the Universe (IPMU)/University of Tokyo, the Korean Participation Group, Lawrence Berkeley National Laboratory, Leibniz Institut für Astrophysik Potsdam (AIP), Max-Planck-Institut für Astronomie (MPIA Heidelberg), Max-Planck-Institut für Astrophysik (MPA Garching), Max-Planck-Institut für Extraterrestrische Physik (MPE), National Astronomical Observatories of China, New Mexico State University, New York University, University of Notre Dame, Observatório Nacional/MCTI, The Ohio State University, Pennsylvania State University, Shanghai Astronomical Observatory, United Kingdom Participation Group, Universidad Nacional Autónoma de México, University of Arizona, University of Colorado Boulder, University of Oxford, University of Portsmouth, University of Utah, University of Virginia, University of Washington, University of Wisconsin, Vanderbilt University, and Yale University.

Software: CYTHON (Behnel et al. 2011), NUMPY (Harris et al. 2020), SCIPY (Virtanen et al. 2020), MATPLOTLIB (Hunter 2007), and COSMOHAMMER (Akeret et al. 2013).

DATA AVAILABILITY

The data underlying this article will be shared on reasonable request to the corresponding author.

REFERENCES

Abdurashidova Z. et al., 2022a, ApJ, 924, 51
Abdurashidova Z. et al., 2022b, ApJ, 925, 221
Akeret J., Seehars S., Amara A., Refregier A., Csillaghy A., 2013, Astron. Comput., 2, 27
Alam S. et al., 2015, ApJS, 219, 12
Asthana S., Haehnelt M. G., Kulkarni G., Aubert D., Bolton J. S., Keating L. C., 2024, preprint (arXiv:2404.06548)
Bañados E. et al., 2019, ApJ, 885, 59
Bañados E. et al., 2018, Nature, 553, 473
Becker G. D., Bolton J. S., Madau P., Pettini M., Ryan-Weber E. V., Venemans B. P., 2015, MNRAS, 447, 3402
Becker G. D. et al., 2019, ApJ, 883, 163
Behnel S., Bradshaw R., Citro C., Dalcin L., Seljebotn D., Smith K., 2011, Comput. Sci. Eng., 13, 31
Bischetti M. et al., 2022, Nature, 605, 244
Bischetti M. et al., 2023, ApJ, 952, 44
Bolton J. S., Haehnelt M. G., Warren S. J., Hewett P. C., Mortlock D. J., Venemans B. P., McMahon R. G., Simpson C., 2011, MNRAS, 416, L70
Bolton J. S., Puchwein E., Sijacki D., Haehnelt M. G., Kim T.-S., Meiksin A., Regan J. A., Viel M., 2017, MNRAS, 464, 897
Bosman S. E. I., Fan X., Jiang L., Reed S., Matsuoka Y., Becker G., Haehnelt M., 2018, MNRAS, 479, 1055
Bosman S. E. I., Ďurovčíková D., Davies F. B., Eilers A.-C., 2021, MNRAS, 503, 2077
Bosman S. E. I. et al., 2022, MNRAS, 514, 55
Chen H. et al., 2022, ApJ, 931, 29
Chen H., Speagle J., Rogers K. K., 2023, preprint (arXiv:2311.16238)
Cranmer K., Brehmer J., Louppe G., 2020, Proc. Natl. Acad. Sci., 117, 30055
D'Aloisio A., McQuinn M., Trac H., 2015, ApJ, 813, L38
D'Odorico V. et al., 2023, MNRAS, 523, 1399
Davies F. B. et al., 2018a, ApJ, 864, 142
Davies F. B. et al., 2018b, ApJ, 864, 143
Davies F. B., Bañados E., Hennawi J. F., Bosman S. E. I., 2023, preprint (arXiv:2312.06747)
Dawson K. S. et al., 2013, AJ, 145, 10
Ďurovčíková D., Katz H., Bosman S. E. I., Davies F. B., Devriendt J., Slyz A., 2020, MNRAS, 493, 4256
Ďurovčíková D. et al., 2024, preprint (arXiv:2401.10328)
Endsley R., Stark D. P., 2022, MNRAS, 511, 6042
Fan X. et al., 2006, AJ, 132, 117
Fathivavsari H., 2020, ApJ, 898, 114
Gaikwad P. et al., 2023, MNRAS, 525, 4093
Garaldi E., Kannan R., Smith A., Springel V., Pakmor R., Vogelsberger M., Hernquist L., 2022, MNRAS, 512, 4909
Ghara R. et al., 2020, MNRAS, 493, 4728
Ghara R., Giri S. K., Ciardi B., Mellema G., Zaroubi S., 2021, MNRAS, 503, 4551
Greig B., Mesinger A., McGreer I. D., Gallerani S., Haiman Z., 2017a, MNRAS, 466, 1814
Greig B., Mesinger A., Haiman Z., Simcoe R. A., 2017b, MNRAS, 466, 4239
Greig B., Mesinger A., Bañados E., 2019, MNRAS, 484, 5094
Greig B., Mesinger A., Koopmans L. V. E., 2020, MNRAS, 491, 1398
Greig B., Trott C. M., Barry N., Mutch S. J., Pindor B., Webster R. L., Wyithe J. S. B., 2021, MNRAS, 500, 5322
Greig B., Mesinger A., Davies F. B., Wang F., Yang J., Hennawi J. F., 2022, MNRAS, 512, 5390
Greig B. et al., 2024, preprint (arXiv:2404.01556)
HERA Collaboration, 2023, ApJ, 945, 124
Harris C. R. et al., 2020, Nature, 585, 357
Hayes M. J., Scarlata C., 2023, ApJ, 954, L14
Heintz K. E. et al., 2023, preprint (arXiv:2306.00647)
Hoag A. et al., 2019, ApJ, 878, 12
Hunter J. D., 2007, Comput. Sci. Eng., 9, 90
Jin X. et al., 2023, ApJ, 942, 59
Jung I. et al., 2022, preprint (arXiv:2212.09850)
Kannan R., Garaldi E., Smith A., Pakmor R., Springel V., Vogelsberger M., Hernquist L., 2022, MNRAS, 511, 4005
Keating L. C., Puchwein E., Haehnelt M. G., 2018, MNRAS, 477, 5501
Keating L. C., Bolton J. S., Cullen F., Haehnelt M. G., Puchwein E., Kulkarni G., 2023, preprint (arXiv:2308.05800)
Keating L. C., Puchwein E., Bolton J. S., Haehnelt M. G., Kulkarni G., 2024, MNRAS, 531, L34
Lewis J. S. W. et al., 2022, MNRAS, 516, 3389
Liu B., Bordoloi R., 2021, MNRAS, 502, 3510
López S. et al., 2016, A&A, 594, A91
Lyke B. W. et al., 2020, ApJS, 250, 8
Mason C. A., Treu T., Dijkstra M., Mesinger A., Trenti M., Pentericci L., de Barros S., Vanzella E., 2018, ApJ, 856, 2
Mason C. A. et al., 2019, MNRAS, 485, 3947
Mazzucchelli C. et al., 2023, A&A, 676, A71
McGreer I. D., Mesinger A., D'Odorico V., 2015, MNRAS, 447, 499
Mertens F. G. et al., 2020, MNRAS, 493, 1662
Mesinger A., Furlanetto S., 2007, ApJ, 669, 663
Mesinger A., Haiman Z., 2007, ApJ, 660, 923
Mesinger A., Furlanetto S., Cen R., 2011, MNRAS, 411, 955
Mesinger A., Aykutalp A., Vanzella E., Pentericci L., Ferrara A., Dijkstra M., 2015, MNRAS, 446, 566
Mesinger A., Greig B., Sobacchi E., 2016, MNRAS, 459, 2342
Miralda-Escudé J., 1998, ApJ, 501, 15
Mondal R. et al., 2020, MNRAS, 498, 4178
Mortlock D. J. et al., 2011, Nature, 474, 616
Murray S., Greig B., Mesinger A., Muñoz J., Qin Y., Park J., Watkinson C., 2020, J. Open Source Softw., 5, 2582
Planck Collaboration XIII, 2016, A&A, 594, A13
Planck Collaboration VI, 2020, A&A, 641, A6
Prochaska J. X., Hennawi J. F., Herbert-Fort S., 2008, ApJ, 675, 1002
Qin Y., Mesinger A., Bosman S. E. I., Viel M., 2021, MNRAS, 506, 2390
Reiman D. M., Tamanas J., Prochaska J. X., Ďurovčíková D., 2020, preprint (arXiv:2006.00615)
Rybicki G. B., Lightman A. P., 1979, Radiative Processes in Astrophysics. Wiley-Interscience, New York
Satyavolu S. et al., 2023, MNRAS, 522, 4918
Saxena A. et al., 2023, A&A, 678, A68
Sobacchi E., Mesinger A., 2015, MNRAS, 453, 1843
Sun Z., Ting Y.-S., Cai Z., 2023, ApJS, 269, 4
Trott C. M. et al., 2020, MNRAS, 493, 4711
Umeda H., Ouchi M., Nakajima K., Harikane Y., Ono Y., Xu Y., Isobe Y., Zhang Y., 2023, preprint (arXiv:2306.00487)
Vernet J. et al., 2011, A&A, 536, A105
Virtanen P. et al., 2020, Nat. Methods, 17, 261
Wang F. et al., 2020, ApJ, 896, 23
Whitler L., Stark D. P., Endsley R., Chen Z., Mason C., Topping M. W., Charlot S., 2024, MNRAS, 529, 855
Witstok J. et al., 2024, A&A, 682, A40
Wold I. G. B. et al., 2022, ApJ, 927, 36
Yang J. et al., 2020, ApJ, 897, L14
Yang J. et al., 2021, ApJ, 923, 262
Zhu Y. et al., 2022, ApJ, 932, 76

APPENDIX A: UPDATED COVARIANCE MATRIX

For this work, we have substantially increased the number of QSOs that are included within our training set for constructing our emission line covariance matrix, from 1673 to 30 166 QSOs. In Fig. A1, we provide an updated correlation coefficient matrix for this new training set to demonstrate the available emission line parameter correlations. Each emission line is separated by solid vertical and horizontal dashed lines, while dashed lines denote the separation between broad and narrow components, respectively. Along the top, each emission line is identified.

This correlation coefficient matrix, $\mathbf{R}_{ij}$ is determined by computing,

$$\mathbf{R}_{ij} = \frac{\mathbf{C}_{ij}}{\sqrt{\mathbf{C}_{ii}\mathbf{C}_{jj}}}, \tag{A1}$$

where the ith and jth subscripts denote the different emission line parameters and $\mathbf{C}_{ij}$ is covariance matrix of the full training set computed using,

$$\mathbf{C}_{ij} = \frac{1}{N-1}\sum_{i}^{N}(\mathbf{X}_i - \boldsymbol{\mu}_i)(\mathbf{X}_j - \boldsymbol{\mu}_j). \tag{A2}$$

Here, $\mathbf{X}_i$ is the data vector containing all ith emission line parameters (21) from the full QSO sample, $\boldsymbol{\mu}$ is its mean and N is the size of our training set.

Generally speaking, we find only very small differences between the line correlation strengths from our updated training set compared to those shown in Greig et al. (2022).

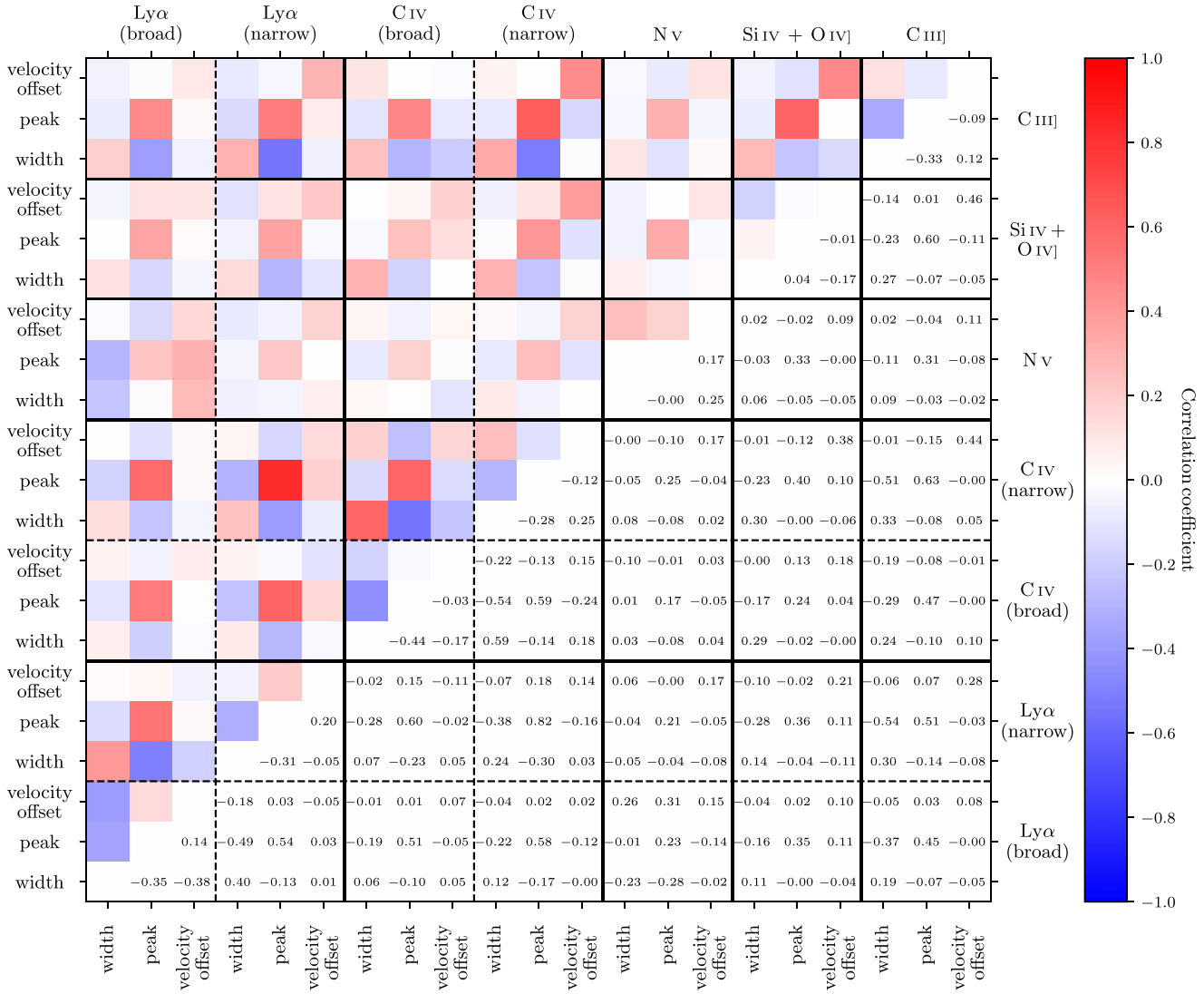

Figure A1. The updated correlation coefficient matrix following the expansion of the training set to 30 166 QSOs with S/N > 6.5 and spanning $2.08 < z < 4.0$ from BOSS DR16Q (Lyke et al. 2020). This 21D matrix highlights the correlation coefficient strengths between the various emission line parameters (separated by solid black vertical and horizontal lines), with the Lyα and C IV lines modelled by a double-component Gaussian and the N V, Si IV + O IV], and C III] lines modelled as a single-component Gaussian. Each emission line component is fully described by three parameters, the peak width, height, and velocity offset from the systemic line centre. The data set used in this work corresponds to an order of magnitude increase over previous work (Greig et al. 2022).

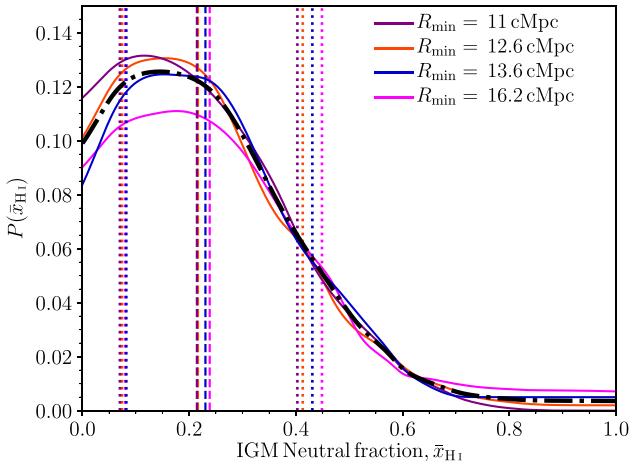

Figure B1. A comparison of the recovered IGM neutral fraction from PSOJ323 + 12 ($z = 6.5872$) after averaging over different minimum H II bubble sizes, $R_{\rm min}$ (black dotted–dashed curve) and when considering each choice of $R_{\rm min}$ individually. In total, we have data available for four choices of $R_{\rm min}$, distinguished by the coloured curves. The vertical dashed lines correspond to the median inferred constraint on the IGM neutral fraction for each individual choice of $R_{\rm min}$, while the dotted lines correspond to the 68th percentile region.

APPENDIX B: IMPACT OF PROXIMITY ZONE SIZE PRIOR

Our constraints on the IGM neutral fraction are determined by averaging over four different minimum local H II bubble sizes, $R_{\rm min}$ (see e.g. Section 3.2 for further details) based on the available data used for our previously analysed $z > 7$ QSOs. Here, we investigate this assumption of averaging over this $R_{\rm min}$ by determining the inferred IGM neutral fraction for a single QSO, PSOJ323 + 12 ($z = 6.5872$) for each individual available $R_{\rm min}$ compared to that obtained when averaging over all four.

In Fig. B1, we provide the inferred IGM neutral fraction PDF following our pipeline outlined in Section 3.5 for an $R_{\rm min}$ of 11 (purple), 12.6 (red), 13.6 (blue), and 16.2 cMpc (magenta). The black dot dashed curve corresponds to averaging over all four choices while the vertical dashed lines correspond to the median of the recovered PDF, whereas the dotted lines denote the 68th percentile uncertainties.

For these different available choices of $R_{\rm min}$, we obtain constraints of $\bar{x}_{\rm H\,I} = 0.21^{+0.18}_{-0.14}$, $0.22^{+0.19}_{-0.15}$, $0.23^{+0.20}_{-0.15}$, and $0.24^{+0.21}_{-0.16}$, respectively. For reference, after averaging we recover $\bar{x}_{\rm H\,I} = 0.23^{+0.19}_{-0.15}$. This implies that for an increasing choice of $R_{\rm min}$, we infer both an increasing IGM neutral fraction and also a broader PDF, which is to be expected. Increasing $R_{\rm min}$ effectively amounts to a marginal leftward shift in the synthetic damping wing profiles in the left panel of Fig. 1. As the distance to the first patch of neutral IGM is larger (for the joint QSO + galaxy contribution), for the same fixed amplitude attenuation (determined by the reconstruction pipeline), we require higher IGM neutral fractions. Equally, due to the increased $R_{\rm min}$, we are sampling further into the tail of the Lyα scattering cross-section, resulting in a lower amplitude variation for fixed wavelength in the synthetic damping wing profiles (reduced scatter in the mean profiles as a function of neutral fraction). This lower width between the damping wing profiles leads to an inferred broadening of the IGM posteriors as the width of our intrinsic profile distribution remains unchanged.

Overall, we recover a shift in the inferred IGM neutral fractions of $\Delta\bar{x}_{\rm H\,I} = 0.022$ for a shift in $R_{\rm min}$ of $\sim$5 cMpc. Additionally, we observe an increase of 0.02 to the inferred 68th percentile region. Therefore, averaging over $R_{\rm min}$ does not have a strong impact on our inferred IGM neutral fraction constraints, especially given the overall width of the 68th percentiles in the posterior.

This paper has been typeset from a TEX/LATEX file prepared by the author.